AGU PUBLICATIONS

JGR

Journal of Geophysical Research: Oceans

RESEARCH ARTICLE

10.1002/2017JC012892

Key Points:
- The tropical ENSO system has a type of universal period doubling cascade route to chaos with low frequency modes and extratropical coupling
- The Heartbeat of the Southern Oscillation is the stable attractor for ENSO; frequency states of ENSO range from 2.5 to 180 years
- Prolonged El Niño (La Niña) period anticipated for 2050–2080 (2018–2026 and 2080–2100)

Supporting Information:
- Supporting Information S1

Correspondence to:
J. T. Bruun,
john.bruun@hotmail.com

Citation:
Bruun, J. T., J. Icarus Allen, and T. J. Smyth (2017), Heartbeat of the Southern Oscillation explains ENSO climatic resonances, *J. Geophys. Res. Oceans*, *122*, 6746–6772, doi:10.1002/2017JC012892.

Received 15 MAR 2017
Accepted 22 JUL 2017
Accepted article online 26 JUL 2017
Published online 28 AUG 2017

Heartbeat of the Southern Oscillation explains ENSO climatic resonances

John T. Bruun[1,2], J. Icarus Allen[3,4], and Timothy J. Smyth[3]

[1]Sweet Briar, Totnes, UK, [2]Formerly at Plymouth Marine Laboratory, The Hoe, Plymouth, UK, [3]Plymouth Marine Laboratory, The Hoe, Plymouth, UK, [4]National Centre for Earth Observation, Plymouth, UK

Abstract The El Niño-Southern Oscillation (ENSO) nonlinear oscillator phenomenon has a far reaching influence on the climate and human activities. The up to 10 year quasi-period cycle of the El Niño and subsequent La Niña is known to be dominated in the tropics by nonlinear physical interaction of wind with the equatorial waveguide in the Pacific. Long-term cyclic phenomena do not feature in the current theory of the ENSO process. We update the theory by assessing low (>10 years) and high (<10 years) frequency coupling using evidence across tropical, extratropical, and Pacific basin scales. We analyze observations and model simulations with a highly accurate method called Dominant Frequency State Analysis (DFSA) to provide evidence of stable ENSO features. The observational data sets of the Southern Oscillation Index (SOI), North Pacific Index Anomaly, and ENSO Sea Surface Temperature Anomaly, as well as a theoretical model all confirm the existence of long-term and short-term climatic cycles of the ENSO process with resonance frequencies of {2.5, 3.8, 5, 12–14, 61–75, 180} years. This fundamental result shows long-term and short-term signal coupling with mode locking across the dominant ENSO dynamics. These dominant oscillation frequency dynamics, defined as ENSO frequency states, contain a stable attractor with three frequencies in resonance allowing us to coin the term Heartbeat of the Southern Oscillation due to its characteristic shape. We predict future ENSO states based on a stable hysteresis scenario of short-term and long-term ENSO oscillations over the next century.

Plain Language Summary The Pacific El Niño-Southern Oscillation (ENSO) nonlinear oscillator phenomenon has a far reaching influence on the climate and our human activities. This work can help predict both long-term and short-term future ENSO events and to assess the risk of future climate hysteresis changes: is the elastic band that regulates the ENSO climate breaking? We update the current theory of the ENSO process with a sophisticated analysis approach (Dominant Frequency State Analysis) to include long-term oscillations (up to 200 years) as well as tropical and extratropical interaction dynamics. The analysis uses instrumental and paleoproxy data records in combination with theoretical models of ENSO. This fundamental result that shows the ENSO phenomenon has a stable tropical Pacific attractor with El Niño and La Niña phases, tropical and extratropical coupling and an intermittency or longer-term form of chaos. We call this attractor the Heartbeat of the Southern Oscillation as the phenomenon is measurable in the Southern Oscillation. We predict future ENSO states based on a stable hysteresis scenario of short-term and long-term ENSO oscillations over the next century.

1. Introduction

Strong El Niño events have widespread and severe economic consequences which are caused by short-term, unpredictable weather system changes and subsequent impacts on the biosphere. It has been estimated that the 1997–1998 El Niño resulted in 22,000 fatalities and $36 billion in economic losses worldwide [*Glantz*, 2001; *Sponberg*, 1999; *McPhaden*, 1999]. However, mechanistic understanding of El Niño and La Niña events is challenging due to the fluctuating and complex nature of the Pacific atmosphere-ocean coupled process [*McPhaden et al.*, 2006; *Cane*, 2005; *Latif et al.*, 1998; *Bjerknes*, 1969]. The El Niño-Southern Oscillation (ENSO) has the appearance of a set of seemingly irregular events that occur through the long-term time record. Since the 1980s, the Tropical Ocean Global Atmosphere (TOGA) research program [*McPhaden et al.*, 1998] has helped establish an ENSO observation and prediction system. A limitation of current ENSO

prediction systems are that they are based on short-term analysis and forecasting methods which characterize the tropical ocean, the relationship between seasonal forcing fluctuations and quasi-cyclicity of typically up to 8 years [*McPhaden et al*., 2006]. Prediction with these methods has a reduction in skill after a 1 year time horizon. *Li et al*. [2013] recently analyzed El Niño modulations, based on a 700 year global reconstruction of tree ring data mapped to the ENSO Sea Surface Temperature Anomaly record. This paleoproxy record has identified a group of characteristic frequencies in the Pacific basin ranging from 2 to 8 years which is consistent with the tropical theory of the ENSO process [*Cane and Zebiak*, 1985]. They also presented spectral evidence of interdecadal ENSO frequencies in the same record. This implies that the ENSO phenomenon also has a basin scale and low frequency dynamic that has been noted before [*Rasmusson et al*., 1990; *Li et al*., 2013]. Tropical and extratropical interaction has recently been discussed in evidence that suggest coupling modulation changes exist going from before to after the 1970s between tropical and extratropical zones [*He et al*., 2013; *Wang and He*, 2012]. A reduced East Asian Winter Monsoon (EAWM) interannual variability and a northward retreat of the EAWM associated climate variability are found to be related to a weakened ENSO-EAWM connection [*Wang and He*, 2012]. *He et al*. [2013] show that there is a Northern Pacific long-term longitudinal dynamic variation in the coupling strength between the tropical ENSO and Northern Pacific atmospheric circulation. By including in ENSO analyses both long-term and basin scale ENSO signals, we are required to confront two assumptions established by *Cane and Zebiak* [1985] about the ENSO phenomena: (a) "*Extratropical influence is not required to be invoked to explain the ENSO process*" and (b) "*The ENSO process is aperiodic*," also called quasi-periodic. The first assumption has enabled the dominant ENSO process; that repeats from a monthly to an 8 year time scale; to be well represented by resolving the wave phenomena along the Pacific equatorial waveguide. The second assumption states that the ENSO system corresponds to a particular class of nonlinear dynamic oscillator. This class of oscillator exhibits quasi-periodic resonances and a quasi-periodic form of chaos, which makes long-term prediction unrealistic. These two assumptions lead to the tropical ocean ENSO theory. Discussion of the nature of the tropical and extratropical connection is important as the connecting mechanisms are not fully understood [*He et al*., 2013; *Trenberth et al*., 1998; *Rasmusson et al*., 1990].

The ENSO system oscillations and resonances are a feature of the combined effect of Pacific basin bathymetry, ocean-atmosphere interaction, and thermodynamic heat flow [*Neelin et al*., 1998; *Cane* and *Zebiak*, 1985; *Tziperman et al*., 1994; *Hoskins and Karoly*, 1981]. One such resonance feature is the quasi-cyclic ENSO mode locking to the seasonal cycle [*Tziperman et al*., 1994]. The nonlinear tropical ENSO process is a type of dynamic system within the class of nonlinear oscillators described by delay oscillators. This delay process is also referred to as a recharge oscillator mechanism. They both represent the same equatorial wave delay process from the perspective of the thermal depletion and recharging of the Pacific warm pool. We refer to them here as a delay oscillator process [*Suarez and Schopf*, 1988; *Battisti and Hirst*, 1989; *An and Jin*, 2004; *Tziperman et al*., 1994, 1995; *Cane and Zebiak*, 1985; *Burgers et al*., 2005].

By establishing the class of oscillator then the underlying ENSO system oscillations and form of chaotic process are better understood and future projection properties can be identified [*Andronov and Khaikin*, 1937; *Tong*, 1990; *Young*, 2011; *Young et al*., 2001]. The Dominant Frequency State Analysis (DFSA) approach we use is novel, highly accurate and can also be mapped into other equivalent climate analyses. This enables the evaluation of theory based on observed data. We carry out a comprehensive signal analysis of the high frequency long-term observational records. Specifically we use Box-Jenkins Time Series Analysis (BJTSA) [*Box and Jenkins*, 1970; *Young*, 2011; *Young et al*., 2001] to analyze the following:

A. Southern Oscillation Index (SOI: 1951–2016).
B. North Pacific Index (NPI: 1899–2016).
C. ENSO SSTA paleoproxy reconstruction data [*Li et al*., 2013] from 1301 to 2005.

The SOI and NPI are both monthly long-term pressure time series. The SOI is widely used to help identify repeating properties of ENSO activity [*Zhang et al*., 1997; *Wolter and Timlin*, 2011; *An and Jin*, 2004; *Yeh et al*., 2009; *Trenberth and Stepaniak*, 2001]. The NPI has been used to analyze longer-term climatic regime shifts [*Minobe*, 1999]. These instrumental records help us assess tropical and extratropical nonlinear interactions. The SSTA record has been systematically cross-checked against Kaplan and HadSST records for the instrumental period 1871–2005 [*Li et al*., 2013; *Kaplan et al*., 1998]. This portion of the series accounts for 59.5% of the SST variance during the instrumental period [*Li et al*., 2013].

The dominant frequencies that are present in the ENSO phenomenon are a natural consequence of the dynamic mechanisms of the ENSO process. We define these dominant frequencies as the frequency states of the ENSO process. We examine the class of oscillator that the ENSO follow by assessing the type of route to chaos and universality it exhibits [*Hilborn*, 2000; *Jin et al*., 1994 ; *Chekroun et al*., 2011; *Dijkstra and Ghil*, 2005; *Bruun et al*., 1995]. In previous research with access to shorter time records, a quasi-period class of ENSO process was identified [*Jin et al*., 1994]. That analysis found that multiple spectral peaks present and their finding was that the dominant spectral peak was a quasi-four year term and not a quasi-two year peak. The system could not represent a period doubling route to chaos as it did not exhibit a universal subharmonic decay structure in its spectrum. As a consequence, the tropical ENSO process appeared to follow a quasi-periodic oscillator structure. Our analysis has a wide scope: we map the ENSO system resonance characteristics and establish the stability of the ENSO system cycles based on the subharmonic properties of the delay oscillator map and the observed frequency states. We show the basin and tropical ENSO system is consistent with a form of period doubling route to chaos modulated by low frequency modes. Using this, we make a prediction of future ENSO climate cycles.

2. Analysis Methods and Data

2.1. Dominant Frequency State Analysis (DFSA)

The analysis of the ENSO is an investigation into the dominant dynamic properties of the ENSO process. To establish the definition of frequency states, we link these states to the mechanisms that form its process. Specifically, a dynamic system is represented by its eigenvalue equation:

$$D\ \psi(\boldsymbol{r},\ t)\ =\lambda\ \psi(\boldsymbol{r},\ t) \tag{1}$$

where D is a differential operator that represents the ENSO phenomenon. For spatial locations $\boldsymbol{r}$ and time t, $\psi(\boldsymbol{r},\ t)$ are the spatiotemporal eigenfunctions that satisfy equation (1). The eigenvalue equation has the property that when operator D acts on the eigenfunction $\psi(\boldsymbol{r},\ t)$ it does not change the nature of the function and the result of applying the operator is simply a scaled scalar value λ times the eigenfunction called its eigenvalue. The eigenvalue equation represents the physical relationship that defines the properties of the dynamical system. The solutions to equation (1) are subject to the natural system boundary conditions, and as a result, the possible eigenvalues λ are generally limited to a discrete set $\lambda_1, \lambda_1, \ldots, \lambda_n$ and/or continuous set over some range. The set of all possible eigenvalues of D is called its spectrum. In general, for dynamical systems, this spectrum can be discrete, continuous or a combination of both. Given a discrete set of n eigenvalues the combination of eigenvalue and eigenvector of equation (1) can be expanded as

$$\lambda\ \psi(\boldsymbol{r},\ t)=\ \sum_{k=1}^{n}\underline{\boldsymbol{f}}_k^s(\boldsymbol{r},t)=\ \underline{\boldsymbol{f}}^s(\boldsymbol{r},t) \tag{2}$$

We denote $\underline{\boldsymbol{f}}^s$ as the combination of all the frequency states for a location $\boldsymbol{r}$ that represents the ENSO dynamic with

$$\underline{\boldsymbol{f}}_k^s(t)=A_k e^{j(\omega_k t+\ \phi_k)}=A_k\{\cos(\omega_k t+\ \phi_k)+i\sin(\omega_k t+\ \phi_k)\} \tag{3}$$

Here ω_k is the frequency of the kth frequency state, ϕ_k is its phase, and A_k is the magnitude of the frequency state and corresponds to the kth eigenvalue. Generally the frequency states are a complex number with real part $\mathrm{Re}\{\underline{\boldsymbol{f}}_k^s(t)\}\ =\ A_k\{\cos(\omega_k t+\ \phi_k)\}$ and imaginary part $\mathrm{Im}\{\underline{\boldsymbol{f}}_k^s(t)\}\ =\ i\ A_k\{\sin(\omega_k t+\ \phi_k)\}$ with $i=\ \sqrt{-1}$.

In Figure 1, we illustrate how DFSA represents the dynamical system for a specified location that is monitored with observational time series. This example has two frequency states $\underline{\boldsymbol{f}}_1$ and $\underline{\boldsymbol{f}}_2$ (Figure 1a), black arrows) that have a periodic resonance related by an integer ratio $\omega_2/\omega_1=1/2$. The radius of each state A_1 and A_2 are the eigenvalues with the phase angles ϕ_1 and ϕ_2 denoting the orientation of the eigenvectors. The time evolution of the eigenvectors move each anticlockwise around the blue circles. This is also shown in Figures 1b and 1c as the trajectory in time being a rotation around a vertical cylinder (with radius A_1 and A_2). Note the second frequency state moves around the circle and cylinder a factor of 2 slower than the first. The combined frequency state $\underline{\boldsymbol{f}}^s=\underline{\boldsymbol{f}}_1+\ \underline{\boldsymbol{f}}_2$ is shown in Figure 1a as the red arrow. As these two states are in periodic resonance the total state has a repeating structure shown as the "double-loop" in Figure 1d.

Due to this periodic resonance, the dynamic has a stable attractor. If the resonance was quasi-periodic then the two states would not have the integer relationship ratio between ω_2/ω_1 and the trajectory in Figure 1d would not repeat. It would instead wobble around this plot, never exactly repeating the path of the trajectory from before. What we observe in nature with a time series is the projection onto the real axis of the frequency states and this is shown in Figure 1e with the periodic resonance appearing as a repeating yet complicated looking cyclic function in time. The empirical spectrum (here we use a periodogram) of the observed time series (Figure 1f) shows the two frequencies of the process.

More generally with DFSA, the observed frequency states of the ENSO process are defined as the real part of equations (2) and (3) and they are typically observed with noise:

$$y(t)=\sum_{k=1}^{n} Re\left\{\underline{\boldsymbol{f}}_k^s(\boldsymbol{r_o},t)\right\}+\eta(\boldsymbol{r_o},t) \tag{4}$$

The $\omega_{process}=\{\omega_1,\omega_2,\ldots,\omega_n\}$ are the identified dominant frequencies at relevant spatial location $\boldsymbol{r}=\boldsymbol{r_o}$ and η is a noise process. For regular and stable characteristic oscillations, the frequencies ω are real. The dominant frequency states correspond to the combined ENSO process eigenvalues and eigenfunctions. The influence of all boundary conditions is implicit in this approach. These together with the dynamic relationship represented by equation (1) give rise to the dominant frequency states. In this method, the focus is on how the dynamical system exhibits its properties through its time evolution. The DFSA approach focuses on the structure of the right-hand side of equation (1). As a consequence, we do not need to explicitly resolve the functional form of operator *D*. In situations where a critical shock to the ENSO climatic system occurs or the system hysteresis changes, decaying frequency modes may also be present. In these cases, the system may transiently or permanently change its frequency states. In these situations, the frequency state (equation (3)) modifies to

$$\underline{\boldsymbol{f}}_k^s(t)=A_k e^{i\left(\omega_{R,k}t+\ \phi_k\right)}e^{-\left(\omega_{I,k}t\right)} \tag{5}$$

where $\omega=\ \omega_R-i\ \omega_I$ has ω_R the stable oscillation and ω_I the rate of decay in time of the decaying frequency mode.

The investigation of the ENSO phenomenon is essentially about identifying the form of the components of equation (1). This is a nontrivial problem and a wide range of forms of the operator *D* have been developed that have

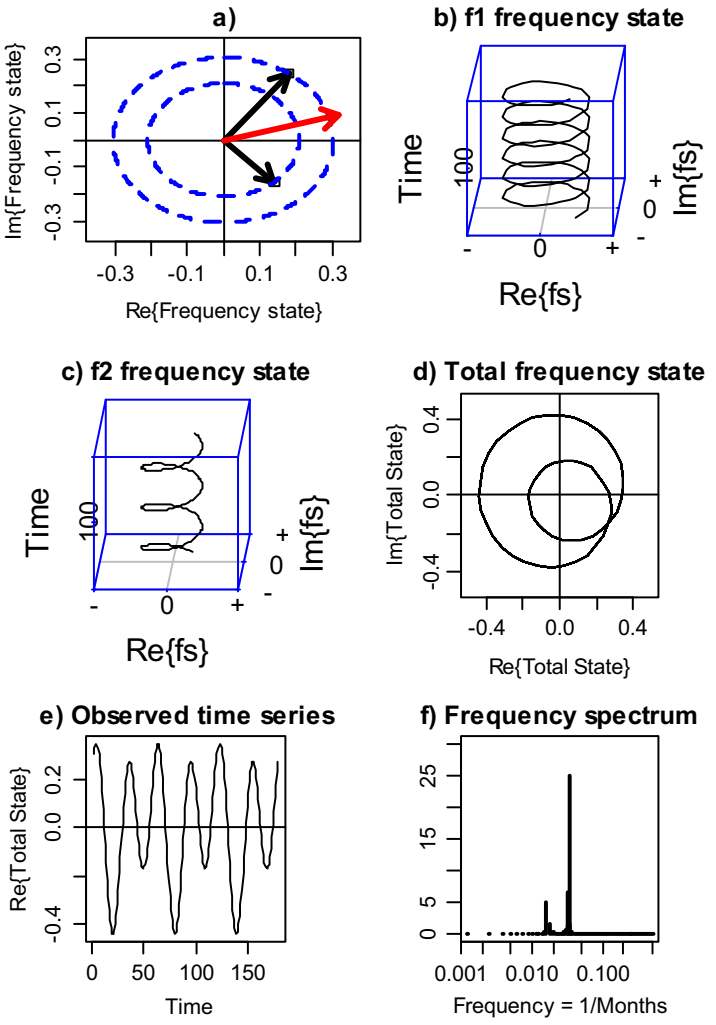

Figure 1. Frequency states analysis connection with dynamic oscillator mechanisms. (a) Eigenvectors $\underline{\boldsymbol{f}}_1$, $\underline{\boldsymbol{f}}_2$ and total combination (red arrow), (b) $\underline{\boldsymbol{f}}_1$ frequency state, (c) $\underline{\boldsymbol{f}}_2$ frequency state, (d) total frequency state (period-three orbit), (e) the observed component of the time series, and (f) the frequency spectrum of the observed time series.

resulted in the tropical ENSO theory such as the delay oscillator and the recharge oscillator representations [*Neelin et al.*, 1998]. The *Cane and Zebiak* [1985] model localizes the analysis to one spatial location and the equatorial longitudinal effect is represented through temporal wave delay terms and mid-Pacific equatorial atmosphere-ocean coupling. In our ENSO analysis, we examine the temporal properties of equation (1) for three spatial scales:

A. For the tropical ENSO process, we use the Southern Oscillation phenomenon.
B. For the tropical and extratropical ENSO process, we examine the Southern Oscillation and its relationship with the North Pacific Index Anomaly.
C. For the Pacific basin ENSO process, we analyze the 700 year SST tree ring paleoproxy record.

We use the tropical ENSO delay oscillator simulation to derive its universal oscillator characteristics. To examine the ENSO process across these three spatial scales and to keep it consistent across the whole time-frequency spectrum, we analyze the right-hand side of equation (1) for the ENSO process as

$$\lambda\ \psi(\boldsymbol{r_o},\ t) = \mathrm{ENSO}(t) : \begin{cases} \boldsymbol{r_o} = \textit{tropical Pacific} \\ \boldsymbol{r_o} = \textit{tropical and extratropical Pacific} \\ \boldsymbol{r_o} = \textit{Pacific basin} \end{cases} \tag{6}$$

The ENSO system dynamic oscillates back and forth around its dominant frequency states. On the extreme edges of the total state trajectory, the system may have a nonlinear response property [see for example, threshold models, *Tong*, 1990; *Bruun and Tawn*, 1998]. This is represented in the DFSA approach as

$$\mathrm{ENSO}(t) = \sum_{k=1}^{n} f_k^s(t) + \eta(t) \text{ for } A_- < \sum_{k=1}^{n} f_k^s(t) < A_+ \tag{7}$$

with $f^s = Re\{\underline{\boldsymbol{f}}^s\}$, time t, n distinct frequency states and random noise $\eta(t)$. The nonlinear response property is captured in the thresholds. The frequency states represent a set of regular oscillations within the total state upper and lower stability thresholds A_+ and A_- . Outside these thresholds, the frequency state representation starts to loose observational skill. The thresholds give information as to the occurrence of extremal processes and edge state transitions. One such threshold situation that could occur in climate systems is where changes in hysteresis are hypothesized due to external shocks or anthropogenic forcing adaptation.

The estimation of ENSO process frequency states f^s from equation (7) requires a highly accurate statistical analysis to identify these from data. The statistical analysis used follows the BJTSA methodology using the following steps [*Box and Jenkins*, 1970; *Young*, 2011; *Young et al.*, 2001]:

A. Identification of dominant frequencies via interpretation of the frequency spectra.
B. Estimation with likelihood inference of the underlying frequency states and accommodating non-ENSO features (noise and trend).
C. Skill assessment of the model.

In step A, the dominant system frequencies ($\omega_{\ process}$) are identified from the time-frequency spectra. The periodogram tool [*Bloomfield*, 2000] is used to quantify the dominant frequency terms. It does this by calculating the importance of each given frequency over a range of frequencies that can be assessed for the time series. A range of enhanced periodogram type tools exist that can be used in the identification step. The multitaper method (MTM) [*Mann and Lees*, 1996; *Ghil et al.*, 2002] is used in the analysis of *Li et al.* [2013]. We use the periodogram tool plus contextual evidence from published work to identify and select the dominant system frequencies. In step B, the model used to derive the underlying frequency states is estimated with likelihood inference. We use BJTSA to allow for the inclusion of additional trends, interventions (such localized non-ENSO processes) and colored noise [*Young*, 2011]. Given an observation y_t of the process at discrete time t going from $t_0,\ t_1,\ t_2,\ \ldots$ to t_{N_T} (here the period between observations is either monthly or annual) the model structure is defined from equations (3) and (7) with BJTSA as

$$y_t = \mu + \sum_{k=1}^{n} f_k(t) + a_T\ T_t' + a_I\ I_t + \eta_t$$

$$f_k(t) = A_k \cos(\omega_k t + \phi_k)$$
$$= A_k \cos\phi_k \cos\omega_k t + A_k(-\sin\phi_k)\sin\omega_k t$$
$$= a_k \cos(\omega_k t) + b_k \sin(\omega_k t)$$
$$\text{where } A_k = \sqrt{a_k^2 + b_k^2} \text{ and } \phi_k = \tan^{-1}\left\{-\frac{b_k}{a_k}\right\} \quad (8)$$

Here μ is the mean of the time series, $f_k(t)$ is the observed frequency state, the function T_t' is a linear increasing function with values $T_{t_0}' = 0$ and $T_{N_T}' = 1$ and the function I_t allows for the inclusion of interventions. The adjacent time point and natural variability is represented by the autoregressive AR(1) noise model:

$$\eta_t = \rho\ \eta_{t-1} + e_t, \ \text{with } e_t \sim N(0, \sigma) \quad (9)$$

This is the red-noise part of the spectrum. Overall the parameters to estimate are $\theta = (\mu, \{a_k, b_k : k = 1, n\}, a_T, a_I, \rho, \sigma)$. With likelihood inference, an objective function called the log likelihood $l(\theta \mid \text{observed data})$ is constructed and used to estimate the parameters θ. In this analysis, it is built from the following:

A. Likelihood estimation provides a concise and The observed data represented in the relationships established in equations (8) and (9).
B. The parameters θ to be estimated.
C. The distribution structure of the underlying random process taken here as Gaussian.
D. The temporal and lagged correlation structure. Using the Box-Jenkins methodology, there is the opportunity to also extend the colored noise process to be an Auto-Regressive Moving-Average (ARMA) structure.

probabilistically sound approach from which to determine the most accurate estimates of the process that is parameterized in the equations. The optimal estimate $\hat{\theta}$ is obtained from the log likelihood as

$$\nabla_\theta\ \hat{l}\left(\hat{\theta} \mid \text{observed data}\right) = 0 \quad (10)$$

This says the maximum likelihood estimate (MLE) $\hat{\theta}$ is the combination of parameter values that are probabilistically the most likely. Asymptotically, the sampling distribution of the MLE is normally distributed (via the central limit theorem). It follows that the MLE is an efficient estimator because its variance is equal to the Cramer-Rao lower bound. In other words, no other estimators can asymptotically be more accurate. A recent discussion and proof of this likelihood inference property is given by *Pawitan* [2013]. This property of parametric likelihood inference tells us that other estimation methods will not asymptotically be more accurate than this approach. The likelihood inference properties together with the identification and estimation steps enable highly accurate analysis of complicated time series model and identification of nonlinear dynamic class structures. The likelihood approach provides the variance estimate of the parameters $\Sigma(\hat{\theta})$ from which confidence intervals are constructed. The variance estimate is derived from the information metric that is represented by curvature of the objective function $l(\theta \mid \text{observed data})$ at $\theta = \hat{\theta}$. The 95% confidence intervals for frequency state coefficients are obtained using the delta method and also more accurate significance testing of the frequency state parameters is carried out with the profile log likelihood [*Coles*, 2001; *Bruun and Tawn*, 1998].

In step C, model skill assessment is carried out. The frequency states represent a regular oscillating system dynamic. The timings and amplitude of the estimated resonances are compared to the observed data with a contingency table to assess the true positive (observation +, model +), true negative (–,–), false positive (–, +), and false negative (+,–) results [*Allen et al.*, 2008]. The skill plot used for our analysis is true positive (threshold) and true negative (threshold) where the threshold is varied from above and below zero to the upper and lower amplitude range of the frequency state values. Where skill increases with increasing threshold value, it shows the percent ability of the frequency state model to represent the dominant resonance spectrum of the ENSO process. The stability thresholds A_+ and A_- of equation (7) are selected in this step as the thresholds above which the frequency states start to loose skill. The estimated frequency states together with the thresholds provide a complete representation of the ENSO dynamical system.

As the DFSA method is an additional and novel method of analysis in climatic science, we briefly discuss the relative advantages of the method as compared to spectral tapering methods, singular spectral analysis and analysis with empirical orthogonal functions. The DFSA method provides the eigenvalue and eigenfunction representation of the phenomenon of study for location(s) of interest. The method has the advantage of being a fully parametric likelihood inference approach so it has asymptotically the most efficient estimation properties that are possible. Other methods can be as accurate however by definition they will not asymptotically be more accurate than DFSA for the identified system. The method enables likelihood significance testing of very subtle and small magnitude effects. The signal structure is estimated in one step and so does not separate low and high frequency bands, resonance coupling, and noise structure into separate analysis steps. The approach has an identified a priori dynamic representation in the form of the dominant frequency signal structure and the nonlinear threshold departure of this and so gives a complete representation of the process. This method does not require an explicit specification of the dynamic operator D (equation (1)) or to resolve the spatial wave structure of the process. All the dynamic information is contained entirely within the regularly sampled time series. This makes DFSA especially suited to climatic analysis where the temporal signal is regular and well represented yet is observed with sparse spatial data coverage.

For investigations of climatic spectra, a range of enhanced spectral methods have been developed that include smoothing and tapering windows applied to the frequency bands [*Mann and Lees*, 1996; *Bloomfield*, 2000; *Ghil et al*., 2002]. These methods enable differing types of signal structure to be accommodated within the estimate of the spectrum. All spectral methods that incorporate a smoothing and/or a tapering window need to balance the spectral resolution capability and the estimate stability. For example, in the situation with two dominant yet fine scale periodic resonance peaks, if the bandwidth of the smoothing and tapering window is larger than the distance between the two resonance peaks the smoothed spectral estimate of these will overlap to form a single peak and so the estimate will fail to resolve the peaks. Where such dominant frequencies are identified DFSA will accurately resolve their contribution in the estimation step. A benefit of smoothing and tapering is that the resulting spectral estimate can be more stable by removing background noise and fine scale structure that detracts from the assessment of the underlying stable signal. The multitaper method (MTM) [*Mann and Lees*, 1996; *Ghil et al*., 2002] is such a form of enhanced spectral method. It is widely used in climatic analysis to help distinguish climatic signals robustly from background red-noise processes as used for example by *Li et al*. [2013]. MTM uses a median smooth of the spectrum to provide a representation of the underlying noise background and then accommodates an autoregressive AR(1) or a red-noise process to give the overall estimated MTM frequency spectrum. With the DFSA method, we do not use any smoothing or tapering assumption to assess and decompose the signal structure. We use the periodogram tool plus contextual evidence from published work to identify and select the dominant system frequencies. In the DFSA method, the red-noise effect is explicitly estimated with the other signal decomposition components in a single estimation step.

Singular Spectrum Analysis (SSA) [*Ghil et al*., 2002] is a method that works well for identifying nonlinear dynamical system properties from short noisy time series. It provides a crude but robust approximation of strange attractor characteristics in the presence of noise. SSA is a data analysis method that is used to extract information without any a priori dynamical knowledge of the physical system. In climatic analysis, SSA is often applied separately to high and low frequency signal bands. Due to its estimation structure, it is in particular very useful to identify and estimate systems that include degenerate eigenvalues (multiple modes with the same frequency) and also those exhibiting quasi-periodic trajectories. Both SSA and DFSA can be applied to the analysis of the process through its time series and does not require explicit spatial data. The advantage of DFSA is that the specific a priori signal structure is estimated accurately in a single step with the most accurate estimator that is asymptotically possible. The DFSA signal representation can also be extended to analyze the effect of frequency state(s) degeneracy where SSA provides strong evidence for the presence of such a degeneracy.

In many situations, where consistently represented spatial and temporal data exist (meteorological weather fields, CMIP simulations, and satellite observations), analyses with empirical orthogonal function (EOF) methods are often used [*Hannachi et al*., 2007]. Standard EOF methods assume a multiplicative time and space functional form and so in particular allow the detailed spatial structure of physical climate fields to be analyzed. Complex and Complex Hilbert EOF's extend the EOF method to incorporate a structured time

signal dimension. The frequency band is sometimes controlled by prior smoothing and the selection of dominant frequencies is generally not part of the EOF approach. DFSA has the advantage of having a richer time signal structure and not requiring spatial-temporal data. In the future, a combination of EOF and DFSA methods would be useful to assess the related spatial structure of Pacific basin (and other) low and high frequency mode coupling mechanisms.

The ENSO signal has dominant frequencies that are assessed with the DFSA approach. Many other phenomena can also be analyzed with DFSA. In situations where multiple physical processes combine together, a decomposition of these components can be investigated with DFSA using the three analysis steps: identification, estimation, and validation. We suggest that DFSA is used together with evidence from SSA, MTM, and EOF's to help build a robust and accurate interpretation of the system process(es). With DFSA, it is incumbent on the climate analyst to ensure that the location(s) of interest can sensibly identify the phenomena of interest, that the process are estimated using a representative signal parameterization and the process phenomena are suitably validated.

2.2. Tropical ENSO Mechanism: The Delay Oscillator

Tziperman et al. [1994] describe the resonance and chaotic properties of the tropical ENSO system using the delay oscillator equation representation [*Cane and Zebiak*, 1985; *Suarez and Schopf*, 1988; *Battisti and Hirst*, 1989]. We refer to this representation as T94. This describes $h(t)$ the thermocline depth deviations from seasonal depth values on the Equator at the eastern Pacific boundary as

$$\frac{dh(t)}{dt} = aA\{h(t-\tau_1)\} - bA\{h(t-\tau_2)\} + c\cos(\omega_a t) \tag{11}$$

$$\tau_1 = \frac{L}{2C_k} \text{ and } \tau_2 = \left(\frac{L}{C_k}\right) + \frac{L}{2C_R} \tag{12}$$

Here t is time, L the basin width, and ω_a is the annual frequency of idealized seasonal forcing. The first term in equation (11) represents the wind-forced Kelvin mode that travels at speed C_k taking delay time τ_1 to reach the eastern boundary from the middle of the basin. The second term in equation (11) represents the westward travelling Rossby wave of speed C_R excited by the wind at the same time for the first term which is reflected as a Kelvin wave and arriving at the eastern boundary at time $t-\tau_2$. The model parameters used in equations (11) and (12) are $C_k = L/2.3$ months, $C_R = C_k/3$, $a = 1/180$ days, $b = 1/120$ days, and $c = 1/138$ days [*Tziperman et al.*, 1994]. The function $A\{h\}$ relates wind stress to SST and SST to the thermocline depth. The nonlinearity of $A\{h\}$ represents the nonuniform stratification of the ocean where the slope of $A\{h\}$ at $h=0$, set by the parameter κ, is a measure of the strength of the coupling between the ocean and atmosphere. The specification of the form of the coupling dynamic established by *Cane and Zebiak* [1985] is crucial to understanding the long-term climatic resonances of this system. It is through the thermocline coupling with the Walker circulation that stable and chaotic tropical Pacific ENSO periodic and quasi-periodic resonances exist. A range of generic functional forms for $A\{h\}$ have been proposed and we use $A\{h\} = \kappa(h - h^3)$ [*Münnich et al.*, 1991]. The bifurcation characteristic varies as the control parameter κ is varied [*Tziperman et al.*, 1994]. This includes periodic mode locking, a cascade to chaos and intermittency. Intermittency in period doubling maps is a form of chaos where the trajectory moves in the neighborhood of a periodic attractor. An example of this is in the threefold bifurcation cascade to chaos of the logistic map [*Feigenbaum*, 1980]. Intermittency in chaos is different to quasi-periodic chaos where resonant frequencies are not related by an integer fraction. With intermittency there is a lower frequency aspect to the spectrum where the trajectory moves in the neighborhood of a periodic attractor. With quasi-periodic chaos there is no periodic attractor structure. What is confusing in the literature is that intermittency is sometimes also referred to as quasi-periodic because being in the neighborhood of a periodic attractor is not strictly periodic. For this analysis, we distinguish between periodic attractor plus intermittency chaos and quasi-periodic chaos. Period doubling patterns have a universal characteristic in the form of the spectrum. For $2n^2$ period doubling cascades, the spectral subharmonic decay has a universal decrease of 8.2 dB per subharmonic [*Feigenbaum*, 1980]. To investigate the universal ENSO bifurcation subharmonic decay structure, we derive the form of the $3n^2$ spectral decay using DFSA as the periodic solutions go from 3, 6, 12, ... bifurcating states toward chaos and also the form of the $3n^2$ plus intermittency or $3n^2 + I$ spectrum. We examine these universal spectra properties for both the logistic map and the T94 tropical ENSO delay oscillator.

Together the spectral information derived from the DFSA and the universal characteristic of the tropical ENSO delay oscillator, we examine the evidence that support a decomposition of the coupling parameter κ into stable, cyclic, and chaotic components as

$$\kappa(t) \sim \kappa^{ST} + \delta\kappa^{Chaotic} + \delta\kappa(t)^{LT} \tag{13}$$

with

A. κ^{ST} representing the short-term (ST) tropical ENSO system stable attractor.
B. $\delta\kappa^{Chaotic}$ the increase in coupling, relative to κ^{ST}, that places the ENSO system in its current weakly chaotic trajectory.
C. $\delta\kappa(t)^{LT}$ is the long-term (LT) attractor precession component in the coupling magnitude.

This extends and enhances the theoretical ENSO description of long-term climatic resonances [*Neelin et al*., 1998].

2.3. Data

We use three observational time series and a set of simulation based time series. All analyses are carried out using the R statistical language [*R Core Team*, 2014]. The data sets are as follows:

A. The Southern Oscillation Index (SOI: 1951–2016, monthly). The SOI series represents the monthly atmospheric air pressure difference between Tahiti and Darwin. This index is widely used to analyze the repeating properties of the ENSO (http://www.ncdc.noaa.gov/teleconnections/enso/indicators/soi/).
B. The North Pacific Index Anomaly (NPIA: 1899–2016, monthly). The North Pacific Index (NPI) is the area-weighted sea level pressure over the region 30°N–65°N, 160°E–140°W. The NPI is defined to measure interannual to decadal variations in the atmosphere-ocean system. From the NPI, we derive the anomaly time series by removing the intraseasonal cycles (12, 6, and 4 months). This is done by applying equation (8) with these frequencies and no AR(1) term to the NPI time series. The NPIA is the residual of that calculation and is then equivalent to the SOI in terms of its cyclic definition (the SOI is a difference of two locations and so the seasonal and within seasonal structure is automatically removed). With its long time series, the NPIA is useful to assess the strength of climatic cycles greater than 30 years (http://www.esrl.noaa.gov/psd/gcos_wgsp/Timeseries/NP/).
C. Sea Surface Temperature Anomaly (SSTA: 1301–2005, annual). The Sea Surface Temperature Anomaly series [*Li et al*., 2013] is a paleoproxy record derived from a 700 year tree ring reconstruction. The raw data for this are 2222 tree ring chronologies from Asia, New Zealand, and North and South America which are mapped into a canonical long-term ENSO time series based on NDJ Nino3.4 SST records. The series is mean corrected for the signal analysis. This paleoproxy record is used to assess decadal to century time scale cycles [*Battisti*, 1995; *Li et al*., 2013; *Lüdecke et al*., 2013] (ftp://ftp.ncdc.noaa.gov/pub/data/paleo/treering/reconstructions/enso-li2013.txt).
D. Logistic map [*Feigenbaum*, 1980]. The logistic map is used to provide the $2n^2$, $3n^2$, and $3n^2+1$ period doubling subharmonic universal features. The map $X_{n+1} = rX_n\ (1-\ X_n\ )$ is simulated with n=1–1000 iterations with control parameter r ranging between 0 and 4.
E. Delay oscillator simulation. The delay oscillator simulation is run by solving equation (11). To separate the stable from the transient parts of the process, we first initialize the simulation with a 1000 year spin-up and then the equation is run for a further 2000 years [*Scheffer*, 2009]. To assess how the resonance characteristic of $h(t)$ vary with κ, multiple samples (>1000) are generated. This tropical ENSO simulation exhibits transitions to chaos of types $3n^2$ and $3n^2+1$. The tropical ENSO universal features of this cascade into chaos are assessed with this simulation for $\kappa = 1.780$ the $3n^2$ period doubling cascade and $\kappa = 1.875$ the $3n^2+1$ to include the tropical ENSO subharmonic and intermittency structure.

3. Results

3.1. Universal Structure of Period Doubling Maps

To derive the temporal subharmonic decay characteristics of the spectrum, we use the logistic map and the T94 delay oscillator bifurcation sequences. Figure 2 show the logistic map and three selected control parameter values r= {3.5682, 3.8493, 3.9}. These correspond to $2n^2$, $3n^2$, and $3n^2 + 1$ (i.e., $3n^2$ plus intermittency). The $2n^2$ subharmonic decay of the eigenvalue spectrum follow the universal result with a

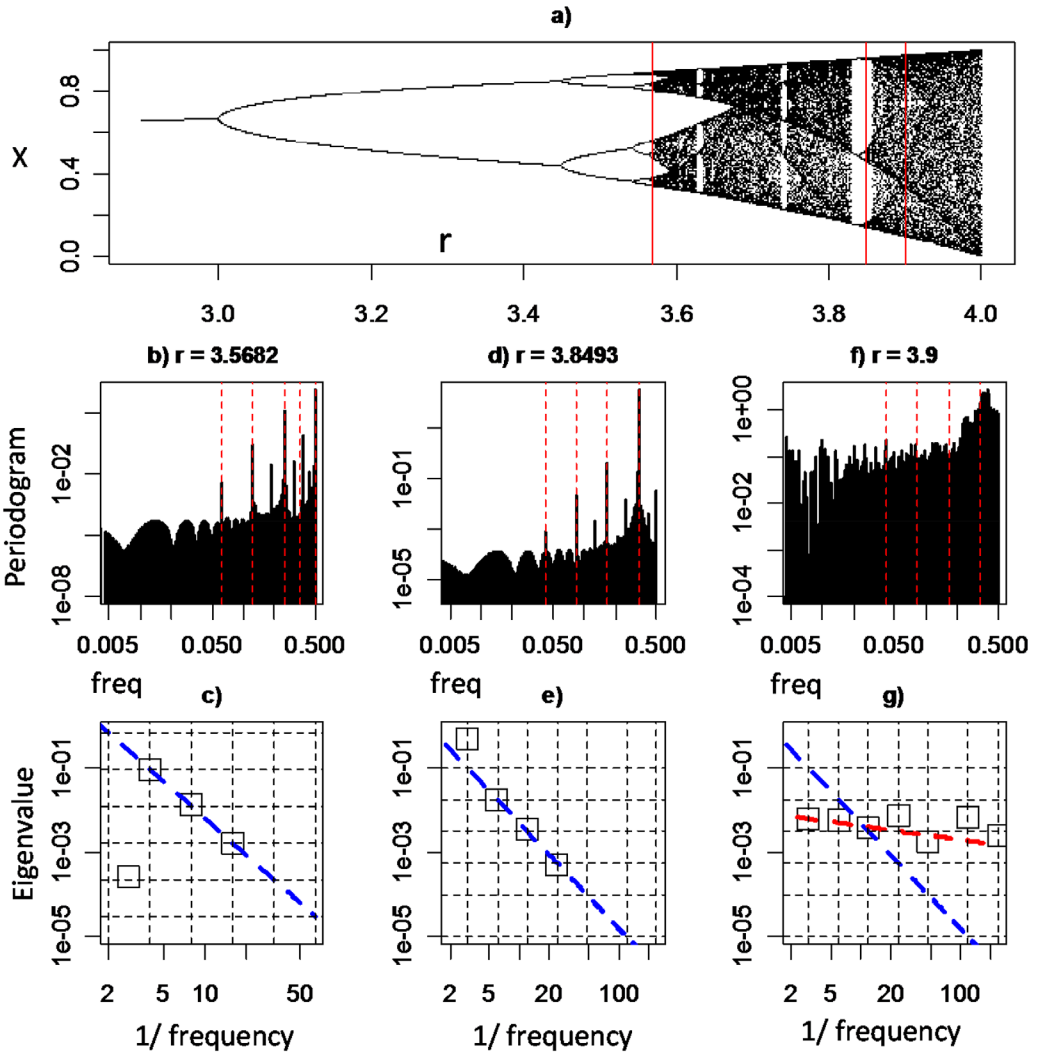

Figure 2. Logistic map universal spectral properties. (a) Bifurcation plot X versus control parameter r. $2n^2$ period doubling characteristic for $r = 3.5682$. (b) Time spectrum with 2, 4, 8, and 16 subharmonic peaks and 2.5 peak highlighted. (c) Eigenvalue of spectrum, the line is the universal power law curve with a drop of 8.7 dB per subharmonic. $3n^2$ period doubling characteristic for $r = 3.8493$. (d) Time spectrum with 3, 6, 12, and 24 subharmonic peaks. (e) Eigenvalue for spectrum, the line is the power law curve with a drop of 7.6 dB per subharmonic. (f, g) For the $3n^2$ period doubling characteristic plus intermittency with $r = 3.9$. The blue line is the power law with a drop 7.6 dB and the red has a drop of 1 dB per subharmonic.

subharmonic decay of 8.7 dB per subharmonic (Figures 2b and 2c), the original analytical result for a $2n^2$ sequence is 8.17 dB [*Feigenbaum*, 1980; *Hilborn*, 2000]. The $3n^2$ subharmonic decay shown in Figures 2d and 2e is a 7.57 dB drop per subharmonic. Moving into the intermittent regime (Figures 2f and 2g), where the underlying periodic attractor still exists but the trajectory jumps about in its neighborhood the spectrum gets flattened and longer duration trajectories arise. This is represented by a decay of 0.99 dB per subharmonic (Figure 2g).

The tropical ENSO bifurcation plot (Figure 3) show how the T94 resonance features change with the coupling interaction κ. With $\kappa = 1$, the atmosphere-ocean is uncoupled and there is no ENSO resonance. Between $\kappa = 1.05$ and 1.3, the system is chaotic and no stable resonances exist. From $\kappa = 1.3$ and up to $\kappa = 1.7$, there are three types of solution with the system resonating at three phase-locked positions. The upper branch corresponds to El Niño (thermocline deepening) and the lower two branches to La Niña (thermocline shallowing). In this range the resonances includes sudden thermocline position jumps that manifest as the broken lines on the plot. Then from $\kappa = 1.7$, the three solutions start a period doubling cascade toward chaos (see insert Figure 3b) starting at about $\kappa = 1.78$. The Feigenbaum constant measures the rate of bifurcation changes [*Feigenbaum*, 1980]. For systems that belong to the universal class of period doubling

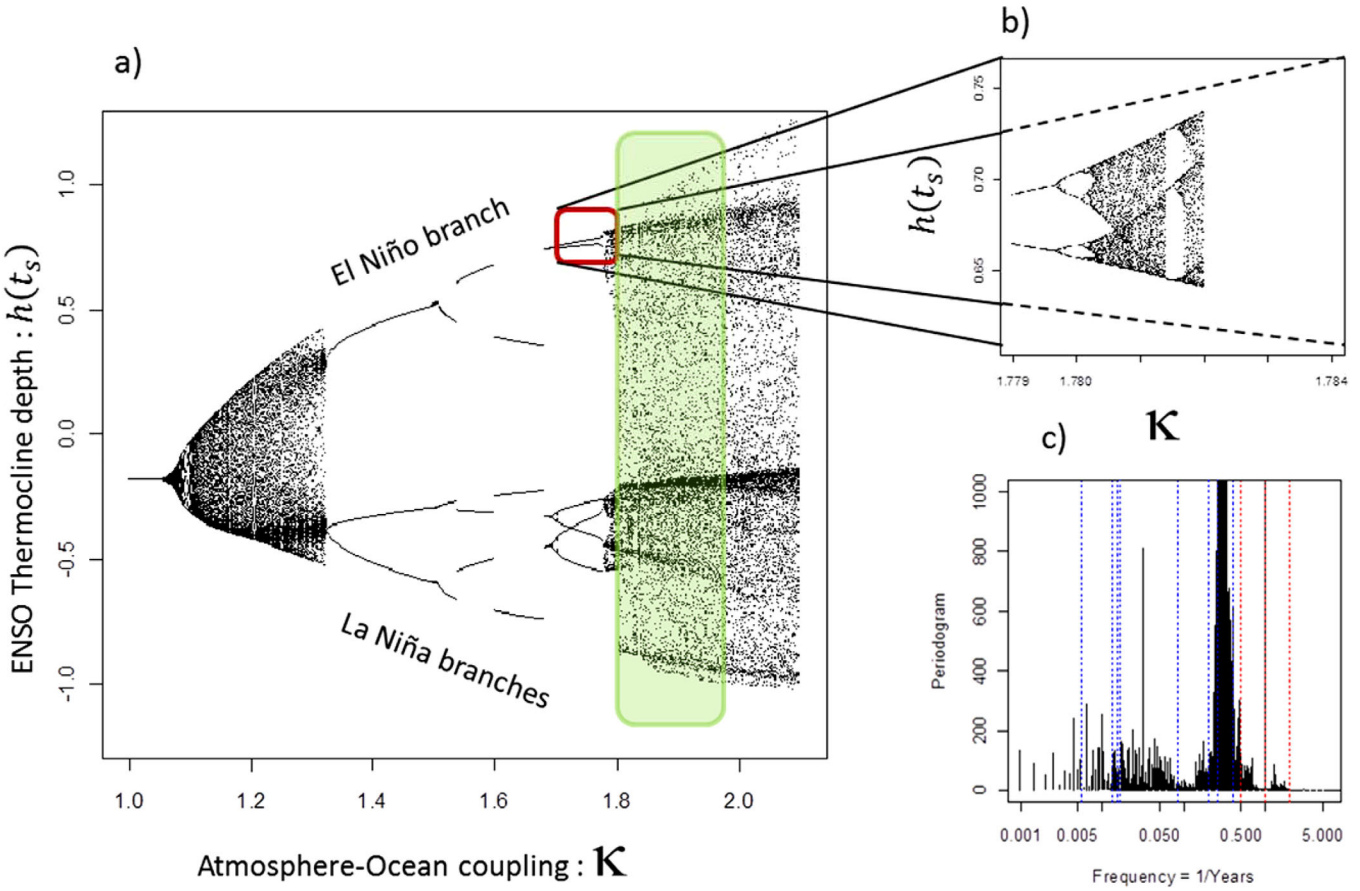

Figure 3. The ENSO resonance characteristic. (a) The bifurcation plot shows the value of $h(t)$ (the solutions to equation (11)) sampled annually at t_s over 2000 years verses changes to the atmosphere-oceanic coupling strength κ. Resonance cycles lasting more than 1 year appear as distinct values on the *y* axis. The upper branch corresponds to the El Niño phase, the lower two branches to the La Niña. The green shaded box is the ENSO current coupling state, (b) this zoom-in shows the period-doubling fractal resonance structure as the system moves from stable resonance frequency states to a mixture of stable and chaotic frequency states. (c) The time-frequency spectrum of $h(t)$ with $\kappa = 1.875$. The ENSO frequencies identified in the observed data-frequency state analysis are shown the blue dotted lines (refer to Figures 5a, 5d, and 5g). The spectrum shows that low frequency states (>10 years) are intrinsic to the ENSO ocean-atmosphere mechanism. The reference vertical lines are for {1/2, 1, 2.5, 3.8, 5, 12, 61, 65, 75, 180} years.

toward chaos, the universal constant of this bifurcation rate is 4.67. Each bifurcation corresponds to a change of system state. These changes of state are exhibited as critical slowing down, a natural state transition feature, which manifests as increased transient fluctuations in the neighborhood of each bifurcation vertex [*Scheffer et al.*, 2009]. We use a 1000 year spin-up to remove the critical slowing down transients so that the bifurcation κ values are clearly identifiable on the cascade toward chaos. The system remains chaotic until κ= 2.13 and then becomes unstable. In Figure 4, we show the T94 delay oscillator subharmonic spectrum characteristic for $\kappa = 1.780$ and 1.875. These are the $3n^2$ bifurcation cascade toward chaos and the $3n^2 + I$ intermittency situation. For $\kappa = 1.780$ (Figure 4a) the subharmonic decay is 11.04 dB per subharmonic. This is steeper than for the $3n^2$ bifurcation cascade of the logistic map and is a new result not previously reported. In the intermittent regime, the subharmonic decay is 0.99 dB per subharmonic so similar to the logistic map. This is a key result: it shows that for the tropical ENSO process in the chaotic regime of a $3n^2 + I$ intermittency situation we can expect to see low frequency subharmonic features. If the chaos is quasi-periodic in the sense that there is not a rational fraction linking resonant frequencies then there will be no low frequency structure. The cascade to chaos, shown in the Figure 3b zoom-in, has a Feigenbaum constant of 4.5 which is close to the 4.67 universal constant. The T94 tropical ENSO process, as described by equation (11), exhibits a subharmonic period doubling route to chaos including low frequency intermittency.

3.2. ENSO Frequency States

The analysis of the frequency states using DFSA for the observational data record is shown in Figure 5. For the 65 year Southern Oscillation Index (SOI) times series (Figures 5a–5c), the frequencies ω_{SOI}= {2.5, 3.8, 5,

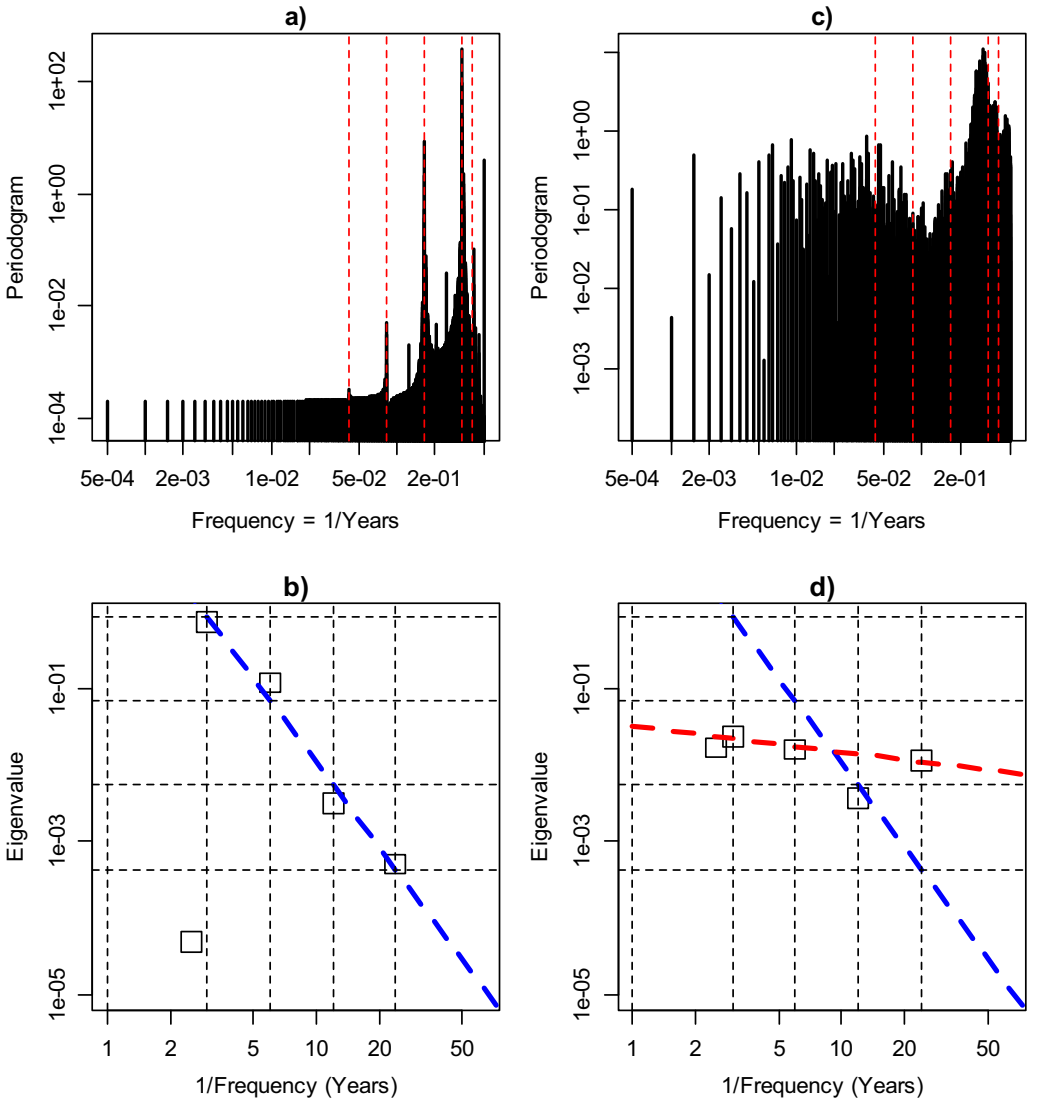

Figure 4. ENSO delay oscillator universal spectral properties. (a) $3n^2$ period doubling characteristic for $\kappa = 1.780$ and (b) eigenvalues of subharmonic sequence the blue line is the power law curve with a drop of 11.0 dB per subharmonic. (c, d) For the $3n^2$ period doubling characteristic plus intermittency with $\kappa = 1.875$. The blue line is the power law with a drop 11.0 dB and the red has a drop of 1 dB per subharmonic.

12, 65} years were identified. These frequency states were found to be statistically significant from the maximum likelihood estimation step. The estimated model is shown in Figure 5b: the blue line with the AR(1) red-noise model, the red line is the underlying frequency state model fit. The skill assessment (Figure 5c) shows that the frequency state representation matches up the timing and intensity of El Niño and La Niña events with skill levels between 65% and 100%. The proportion of true negatives range from 65% for small amplitude negative SOI events to 90–100% for the large extreme El Niño events. This is shown by the skill increasing in accuracy as the threshold varies from 0 to 0.7. There is a similar increasing skill characteristic for the true positive events with the skill level ranging from 65% for small positive SOI values to 75% for large La Niña events.

From the 117 year North Pacific Index Anomaly times series (Figures 5d–5f), the frequencies ω_{NPIA}={5.8, 14, 61} years were identified and found to be statistically significant. The estimated model is shown in Figure 5e: the blue line with the AR(1) red-noise model, the red line is the underlying frequency state model fit. The inclusion of a very marginally significant negative trend to the frequency state model could be a feature of a low frequency cycle and is shown by the green line. The skill assessment (Figure 5f) shows the

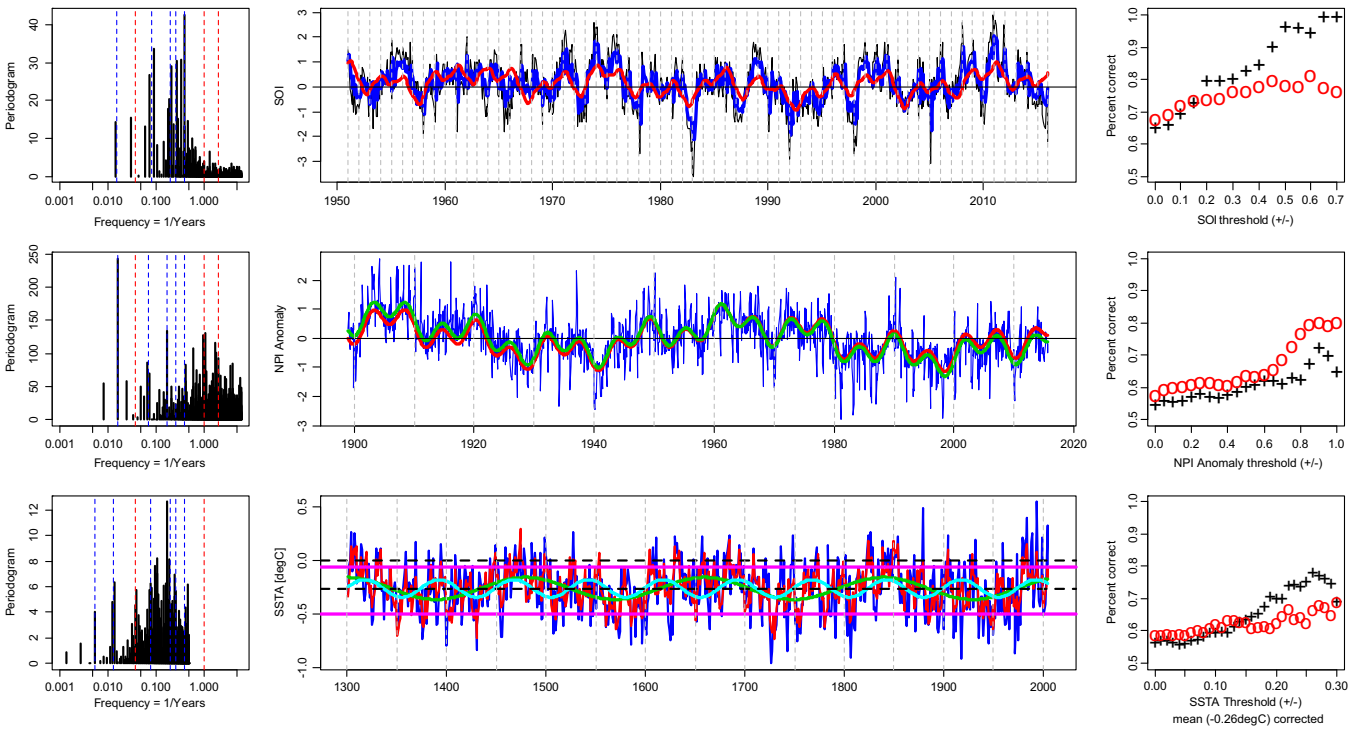

Figure 5. Frequency states of the ENSO process. Using BJTSA this shows the identification of dominant frequencies from data, the estimated frequency state models and the frequency state model skill assessment verses data. Southern Oscillation analysis: (a) spectrum, ω_{SOI} = {2.5, 3.8, 5, 12, 65} years; (b) SOI (black lines), estimated model (blue line including red-noise, AR(1), red line – the underlying combined frequency states), and (c) skill assessment true positive (red circles) and true negative (black +) verses increasing |SOI| threshold. North Pacific Index Anomaly analysis: (d) spectrum, ω_{NPIA} ={5.8, 14, 61} years; (e) estimated model: blue line including red-noise, AR(1), red line – the underlying combined frequency states, green line, the additional effect of including a trend, (f) skill assessment true positive (red circles) and true negative (black +) verses increasing |NPIA| threshold. Sea Surface Temperature Anomaly analysis: (g) spectrum, ω_{SSTA} ={2.5, 3.8, 5, 13, 27, 75, 180} years; (h) estimated model: blue line including red-noise, AR(1), red line – the underlying combined frequency states, light blue line, the 75 year frequency state, green line the 180 year frequency state. Solid thick purple lines show the thresholds indicated by skill analysis within which the frequency state models hold. (i) Skill assessment true positive (red circles) and true negative (black +) verses increasing |SSTA| threshold.

frequency state representation matches the timing and intensity of true positive and true negative events with skills between 55% and 85%. The skill plateaus for positive events and declines for negative events outside a threshold level of |NPIA| > 0.9. This indicates a level of system asymmetry between the positive and negative phases represented by the NPIA representation of the ENSO process. Outside these thresholds, the events could correspond to situations where the stable climatic hysteresis may be adjusted.

The analysis of the 705 year Sea Surface Temperature Anomaly data is shown in Figures 5g–5i. The frequencies ω_{SSTA} ={2.5, 3.8, 5, 13, 27, 75, 180} years were identified. The frequencies up to 75 years were also found to be statistically significant by *Li et al.* [2013] by applying MTM and long-term spectral analyses. The shorter frequencies (2.5–12 years) identified by *Li et al.* [2013] match those from this SOI analysis to within ±10% in period magnitude. Figure 5g also shows that the 180, 75, and 27 year frequencies clearly stand out. The estimated model is shown in Figure 5h: the blue line with the AR(1) red-noise model, and the red line is the underlying frequency state model fit using DFSA. The skill assessment (Figure 5i) shows the frequency state representation matches up the timing and intensity of true positive and true negative events with skill levels between 55% and 80%. For true negative events the skill increases from 55% to 80% as the SSTA threshold changes from the long-term mean of −0.26°C down to −0.5°C. The true negative skill decreases for temperatures colder than °0.5°C. For true positive events, the pattern is similar and the skill breaks down with a flat plateau for SSTA temperatures above −0.06°C. Again this indicates a level of system asymmetry between the positive and negative phases. The positive phase (circles in Figure 5i) also show the skill then increases above −0.06°C which could indicate hysteresis stability outside the upper SSTA threshold.

3.3. ENSO Frequency State Eigenvalues and Eigenvectors

In Figures 6–8, we show the DFSA eigenvalue and eigenvector analyses of the frequency states for the SOI, NPIA, and SSTA shown in Figure 5. These figures show (a) the frequency states, (b) the eigenvalues verses

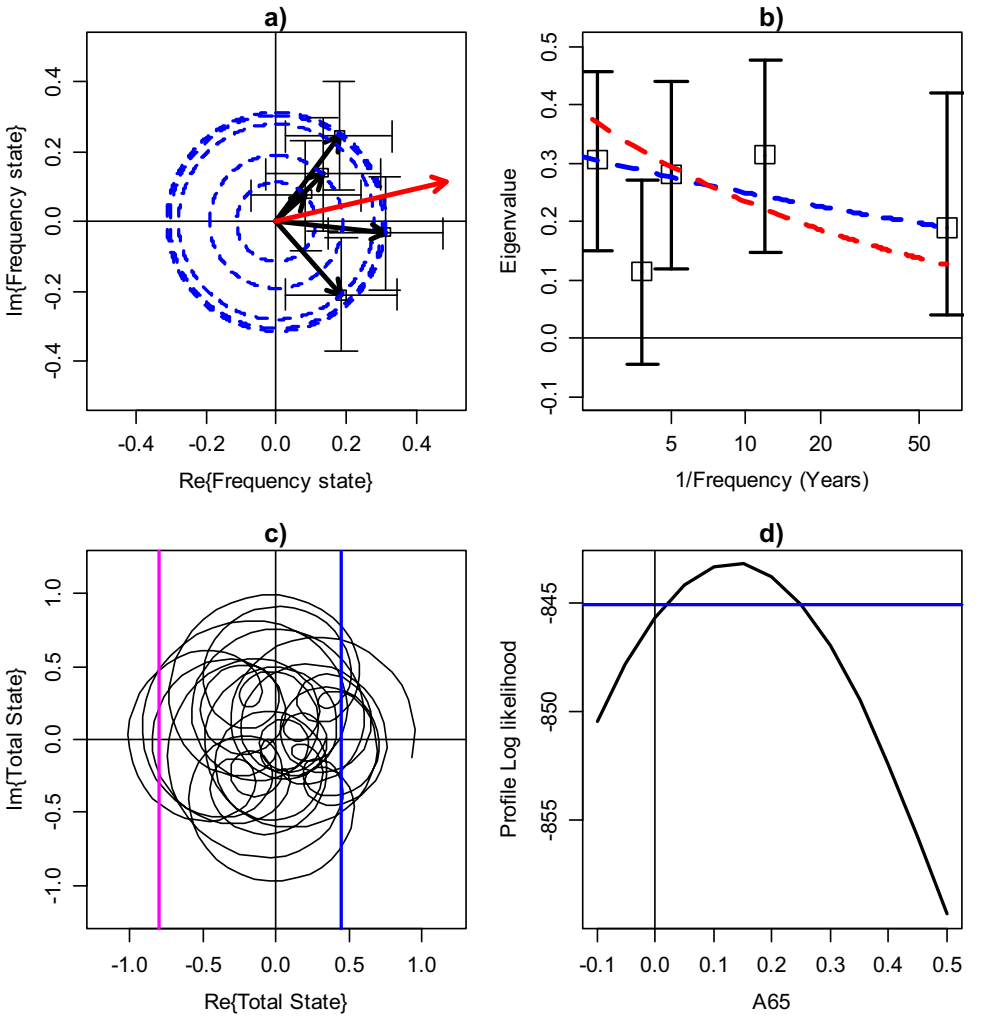

Figure 6. Eigenvalue and function analysis of the Southern Oscillation frequency states $f^{SOI}_{\omega_k}$, $\omega_k = \{2.5,\ 3.8,\ 5,\ 12,\ 65\}$. (a) Eigenfunctions of the frequency states (approx. 95% confidence intervals). Each function will rotate in time around the blue circles with the period of its characteristic frequency. The total SO frequency state f^{SOI} is the red arrow (scaled in this plot to have amplitude of $^1/_2$). (b) Eigenvalues (with 95% CI) for each of the SOI frequency states. The dotted line shows how eigenvalues decrease as the frequencies get longer (red line is a drop of 1 dB and blue 0.44 dB per subharmonic. (c) Total state trajectory, with upper (lower) skill threshold A_+ (A_-) depicted as blue (pink). (d) Profile log likelihood of the low frequency eigenvalue A_{65} along the direction of the vector. The blue horizontal line denotes a drop of 3.84/2 from the optimal likelihood: the crossing points of the blue line with the log likelihood are the 95% confidence interval.

time period, (c) the total state trajectory, and (d) the profile log likelihood for key low or high frequency coefficients (SOI: low frequency; NPIA: high frequency; and SSTA: low frequency). For the SOI analysis (Figure 6b), the 2.5, 5, and 65 year eigenvalues exhibit the characteristic of a subharmonic decay. This subharmonic decay has a magnitude of 0.44 dB per subharmonic (blue dashed line). The red dashed line is the 0.99 dB per subharmonic line found for the T94 delay oscillator in its $3n^2 + 1$ regime. It suggests that the universal subharmonic decay rate in the observed Southern Oscillation is slower than is obtained from the T94 tropical ENSO theory. The profile log likelihood (Figure 6d) for the low frequency eigenvalue A_{65} shows this is statistically significant at the 5% level. This is a major finding. The tropical ENSO process exhibit a characteristic that is consistent with a periodic subharmonic spectral structure and low frequency coupling. This has not been identified and accurately estimated before and so previously the tropical ENSO dynamic was thought to exhibit quasi-periodicity. The 3.8 year frequency state eigenvalue has a magnitude that is about 1/2 to 1/3 that of the other frequency states. Its statistical significance is weaker than for the other states. The 3.8 year frequency state is also not in a periodic resonance with the other frequency states. We retain this state in our DFSA as it represents a part of the weakly chaotic tropical ENSO trajectory. Interestingly the 12 year eigenvalue is larger than the subharmonic decay curve. This could mean that there is a partial,

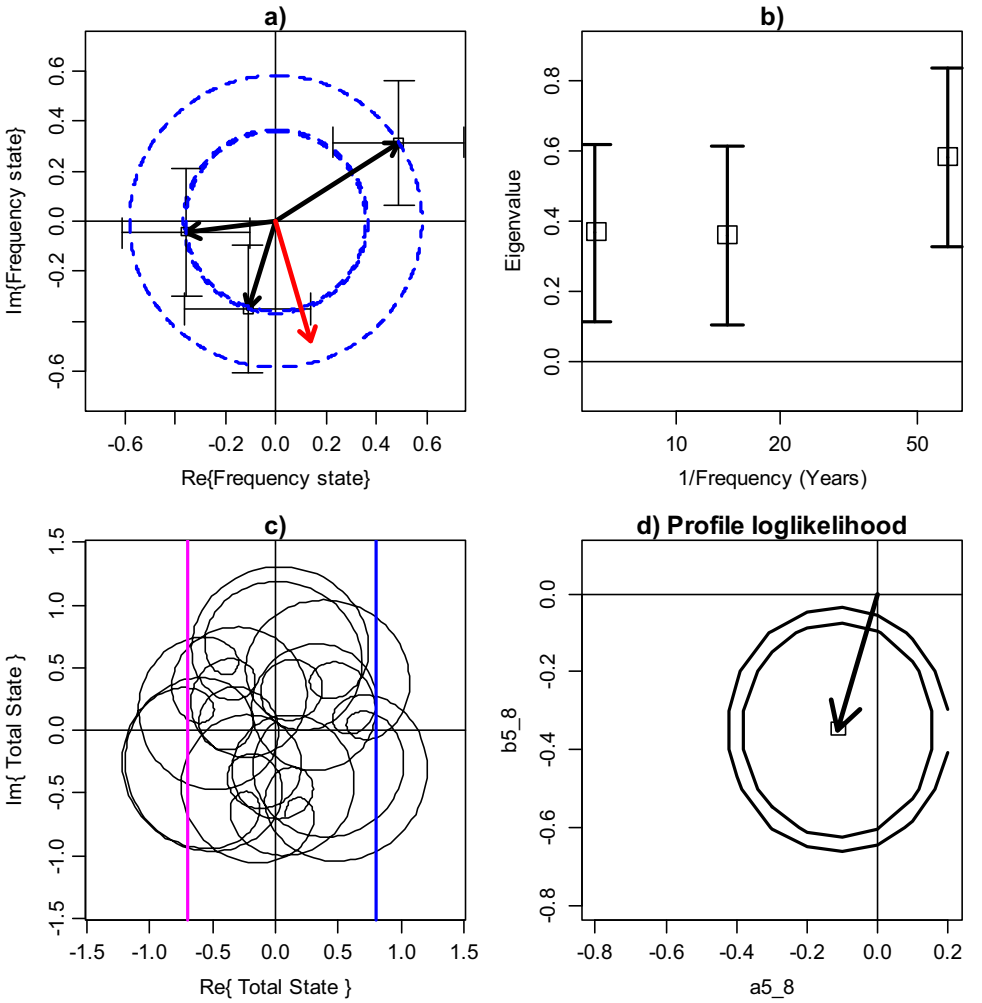

Figure 7. Eigenvalue and function analysis of the North Pacific Index Anomaly frequency states $f^{NPIA}_{\omega_k}$, $\omega_k = \{5.8,\ 14,\ 61\}$. (a) Eigenfunctions of the frequency states (approx. 95% confidence intervals). Each function will rotate in time around the blue circles with the period of its characteristic frequency. The total NPIA frequency state f^{NPIA} is the red arrow (scaled in this plot to have amplitude of $1/2$). (b) Eigenvalues (with 95% CI) for each of the NPIA frequency states. (c) Total state trajectory, with upper (lower) skill threshold A_+ (A_-) depicted as blue (pink). (d) Profile log likelihood of frequency state $f_{5.8}$ coefficients $(a_{5.8},\ b_{5.8})$. The two circles represent the 95% (inner circle) and 90% (outer circle) confidence region of these coefficients and represent a drop of 5.99/2 and 7.81/2 from the optimal log likelihood.

quasi-periodic coupling with a 12 year cycle, and that the 12 year frequency state is also excited by external forcing. *Li et al.* [2013] found that there was a meandering phase-modulation with the solar cycle. Perhaps part of the 12 year cycle is linked to ENSO resonance and part to external solar forcing such that the solar forcing additionally excites the 12 year ENSO frequency state. We do not evaluate this point here but note it as a potential hypothesis for future research.

The NPIA region (Figure 7) has three clearly defined frequency states. In particular, the high frequency 5.8 year state is statistically significant (at a 5% level) which shows that both low and high frequency modes are part of this extratropical process. Due to the property of slow ocean dynamic adjustment [*Jin*, 1997], the higher frequency tropical ENSO signal will be absorbed by the extratropical gyre dynamic. The slow ocean dynamic adjustment acts as a low pass filter, and so the higher frequency tropical signal as it passes into the extratropical zone will be "smeared" into a lower frequency band. We see this here as the significant 5.8 year frequency state (Figures 7b and 7d). This represents the higher frequency part of the tropical ENSO signal that has been transmitted into the subtropics. The analysis also shows a 14 year frequency state. Perhaps the slow ocean adjustment also filters the 12 year equatorial frequency state to help produce a subtropical 14 year frequency state. Interestingly, the 61 year low frequency state has the largest eigenvalue with magnitude about 50% larger than for the other two. This shows that the (Northern) extratropical

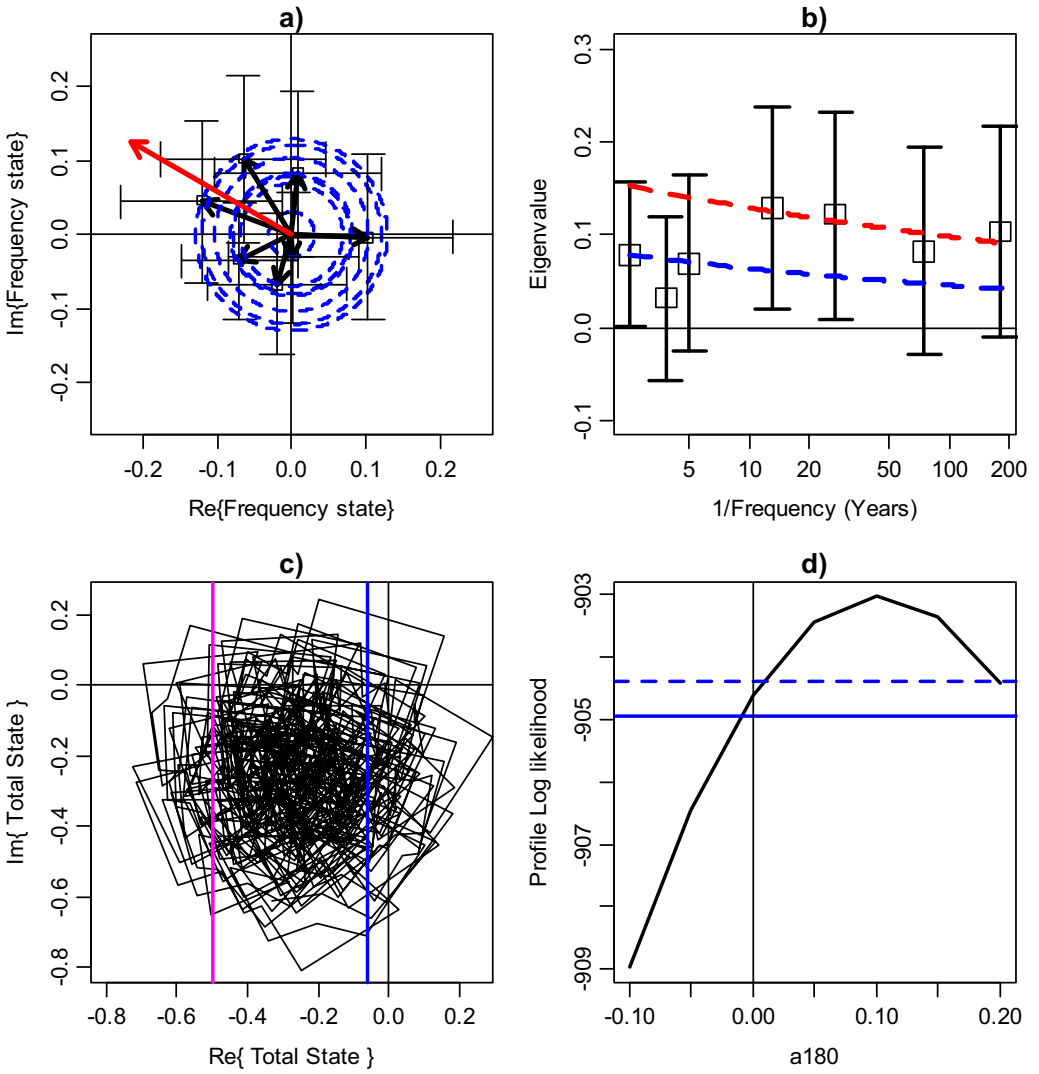

Figure 8. Eigenvalue and function analysis of the tree ring reconstruction Sea Surface Temperature Anomaly frequency states $f^{SSTA}_{\omega_k}$, $\omega_k = \{2.5, 3.8, 5, 13, 27, 75, 180\}$. (a) Eigenfunctions of the frequency states (approx. 95% confidence intervals). Each function will rotate in time around the blue circles with the period of its characteristic frequency. The total SSTA frequency state f^{SSTA} is the red arrow (scaled in this plot to have amplitude of 1/4). (b) Eigenvalues (with 95% CI) for each of the SSTA frequency states, the blue and red curves are for subharmonic drop of 0.36 dB per subharmonic. (c) Total state trajectory, with upper (lower) skill threshold A_+ (A_-) depicted as blue (pink). (d) Profile log likelihood of the higher frequency eigenvalue coefficients (a_{180}, b_{180}). The solid (dashed) blue horizontal line denotes a drop of 3.84/2 (2.71/2) from the optimal log likelihood: the crossing points of the blue line with the log likelihood is the 95% (90%) confidence region.

region has both a dominant low frequency mode and significant higher frequency modes. Figure 7c shows the combined frequency state trajectory. These frequency states are not linked directly by a periodic resonance relationship so the quasi-period trajectory meanders around the three frequencies of the NPIA. The tropical ENSO subharmonic structure is present in the extratropics through the way the tropics and extratropics couple together.

The SSTA paleoproxy data analysis is shown in Figure 8. Due to the methodology of calculating the long-term SSTA series from paleoproxy data, we do not expect the results to be as accurate as for the pressure based instrumental analyses shown in Figures 6 and 7 [*Battisti*, 1995]. However, the SSTA analysis is an essential part of establishing the properties of the high and low frequency basin scale characteristics. This record provides a 700 year time scale for this analysis. The eigenvalues (Figure 8b) show the same high frequency structure as for the SOI (Figure 6b). With the SSTA, the lower frequency states dominate the eigenvalue spectrum with the 13, 27, and 180 year eigenvalues being the largest. The 180 year frequency state

has a significance of $p = 0.10$ derived from the profile log likelihood (Figure 8d). The subharmonic decay we noted for the SOI data is evident here with value 0.36 dB per subharmonic. This decay characteristic is plotted twice in Figure 8b, one curve for the high frequency (2.5 and 5 year) and the other for the low frequency (13, 27, 75, and 180 year) spectrum components (y axis intercept chosen to align the curves). This decay of 0.36 dB per subharmonic is similar in magnitude to the 0.44 dB per subharmonic noted above for the tropical ENSO signal using the SOI instrumental based data. This paleoproxy retains the impact of the tropical ENSO signal on the Pacific basin tree ring growth pattern. The basin scale ENSO phenomenon is a combination of both the interconnected tropical and extratropical ENSO processes. The instrumental tropical ENSO basin record shows the existence of significant subharmonic and low frequency structure. The paleoproxy results also exhibit this subharmonic decay structure, albeit with a lower level of accuracy that is anticipated for evidence emerging from paleoproxy data.

3.4. ENSO Frequency State and Trend Decomposition

The estimates from the observational data provide the frequency states of the ENSO process. Through the combination of applying equations (7) and (8) the estimated frequency states f^s for the time series shown in Figure 5 are

$$f^s_{SOI} = f_{2.5} + f_{3.8} + f_5 + f_{12} + f_{65} + Trend_{SOI} \tag{14}$$

$$f^s_{NPIA} = f_{5.8} + f_{14} + f_{61} + Trend_{NPIA} \tag{15}$$

$$f^s_{SSTA} = f_{2.5} + f_{3.8} + f_5 + f_{13} + f_{27} + f_{75} + f_{180} + Trend_{SSTA} \tag{16}$$

The process is dominated by the system resonances that form the cyclic components of the frequency states. In this notation, f_T is the frequency state component (equation (8)) with a cycle period of T years. We account for a potential trend relative to the other cycles, which can manifest as an underlying change or a segment of an ultra-low frequency oscillation with wavelength longer than the observational data set or a combination of both.

Table 1 shows the trend decomposition of the three frequency state models. In the SOI and SSTA cases, the effect of including a trend is not statistically significant. For the NPIA, the apparent trend is a negative 9.7% effect but it is only of very marginally statistically significance (p-value = 0.126). The $Trend_{SSTA}$ term is positive and not statistically significant at a 10% level, indicating that there is not strong trend existence evidence in the 700 year SSTA data. The marginal trend seen in the NPIA series may well be a feature of the 180 year frequency state (noted in the SSTA analysis) going from its negative to positive phase over 1900–2000. The apparent 10% negative trend effect for the NPIA looks like it could be associated with an up to 0.5°C SSTA temperature increase with f^s_{SSTA} values ranging from $<$–0.5°C over 1900–1970s to $>$0.0°C from 1970s onward. Overall, the estimated trend terms in the frequency states are small and appear to be negligible.

3.5. ENSO Characteristic Phase Space of Frequency States

The phase space helps us to distinguish underlying cyclic based bifurcations from low frequency cycles and the chaotic aspects of the process. In Figure 9a, we show the combination of $f_{2.5} + f_5$ from the SOI model as our representation of the tropical ENSO process together with the raw SOI data. The deep negative phase is the El Niño and the two positive phases are the La Niña events. These states correspond to the stable period-three attractor state on the Figure 3a bifurcation plot with κ in the range 1.33–1.7. In Figure 9b, we plot f_5 verses $f_{2.5}$. This is the high frequency phase space of the underlying stable attractor. The deep negative El Niño (positive La Niña) phase corresponds to the combination of f_5 and $f_{2.5}$ that is below (above) the diagonal line. It is worth noting that the La Niña phase includes a brief small

Table 1. Frequency State Trend Decomposition[a]

	RMS Ratio Index	%Trend (1 *d.p.*)	Trend Significance (*p*-Value)
SOI	$RMS(f^s_{SOI})/RMS(f^s_{SOI} - Trend_{SOI}) = 1.035957$	3.6	0.616
NPIA	$RMS(f^s_{NPIA})/RMS(f^s_{NPIA} - Trend_{NPIA}) = 1.097262$	9.7	0.126
SSTA	$RMS(f^s_{SSTA})/RMS(f^s_{SSTA} - Trend_{SSTA}) = 1.00016$	0.0	0.950

[a]RMS Ratio Index is the ratio of the Root-Mean-Square (RMS) of the frequency states including the cycles and trend over the RMS of the cyclic frequency states without the trend. The %Trend component of the signal is calculated as (RMS Ratio Index – 1) × 100. The trend statistical significance p-value (using a two-sided test setting verses no trend) is obtained from the estimated trend coefficients and standard errors of equation (8).

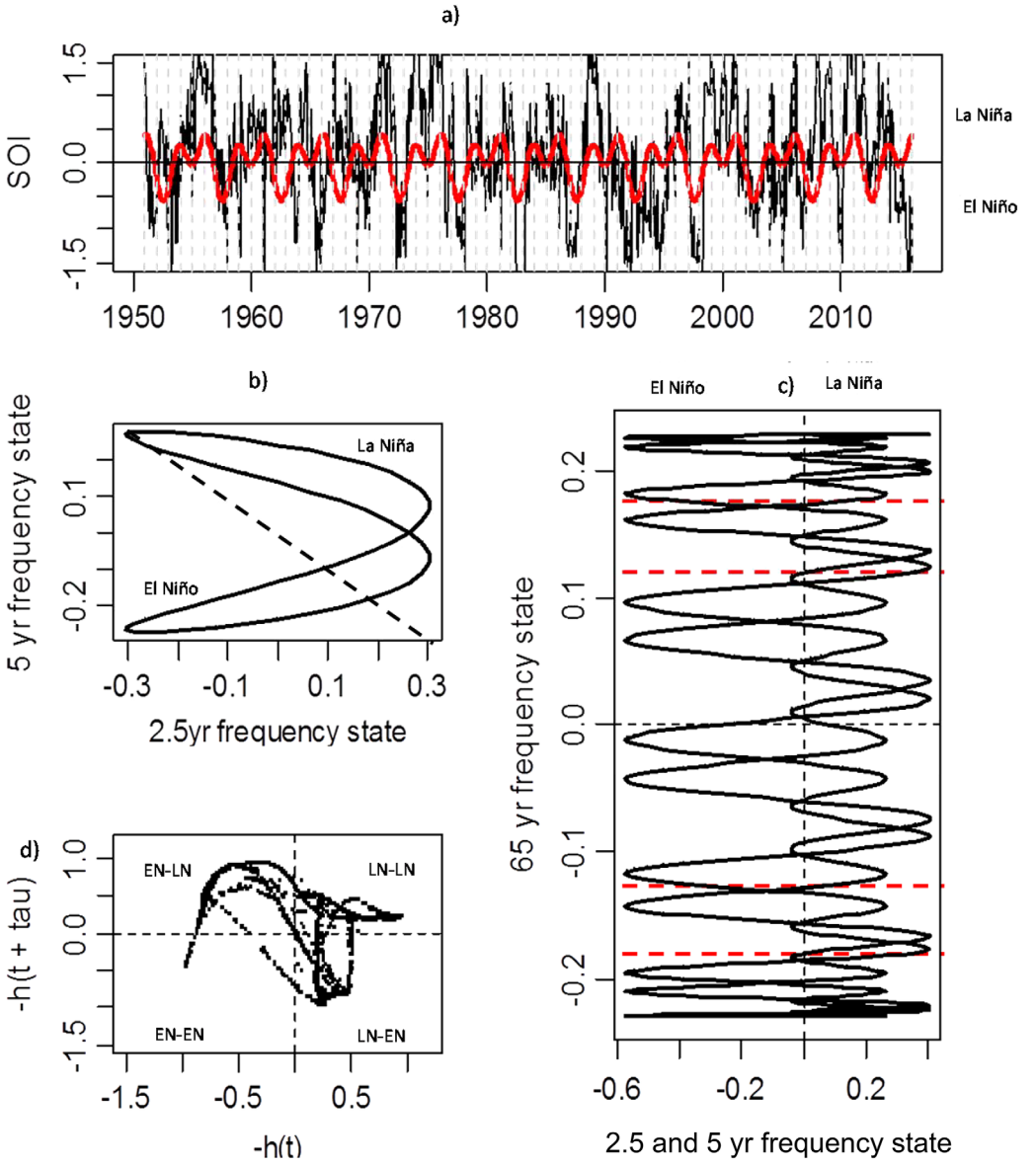

Figure 9. Phase space of the ENSO frequency state model. (a) Time series of SOI (black line) with short-term Heartbeat frequency state (red line), (b) phase space of 2.5 and 5 year frequency states, (c) Heartbeat of the Southern Oscillation stable attractor: the combined 2.5 and 5 year and 65 year frequency states both estimated from the SOI. Distinct and large El Niño (La Niña) phases correspond to the persistently negative (positive) phase sectors. (d) Dynamic ENSO model (equation (11) with $\kappa = 1.875$) sampled with $\tau = 1$ year, the top left and bottom right quadrants are where the system exhibits transition resonance properties: La Niña to El Niño (LA-EN), persistent El Niño (EN-EN), El Niño to La Niña (EN-LN) and persistent La Niña (LN-LN).

negative minimum on this plot: the phases and duration of the La Niña manifest as a more subtle and complicated timing component of the ENSO process. The 65 year frequency state f_{65} verses $f_{2.5}+f_5$ is shown in Figure 9c. The positive and negative states of this 65 year term are also clearly apparent from the NPIA analysis shown in Figures 5d–5f. This shows the periodic precession of the low frequency cycle. There are distinct long-term cyclic event changes to the total frequency state as it moves through a whole long-term cycle.

Due to the characteristic shape of the 2.5, 5, and 65 year frequency states that form a mode locked resonance, we coin the phrase the Heartbeat of the Southern Oscillation to describe this mode locked state. This is the tropical ENSO attractor state. In Figure 9c, we see the positive and negative phases of the 65 year frequency state. In particular for $f_{65} \geq 0$, the system transitions from a negative to positive f^s_{SOI} state and

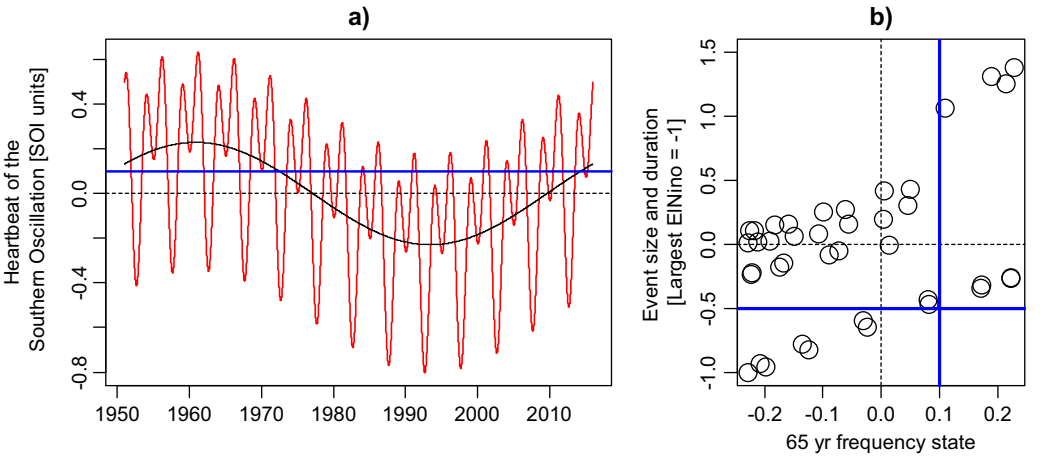

Figure 10. ENSO modulation characteristic derived from SOI. (a) Heartbeat of the Southern Oscillation attractor (red line), with low frequency 65 year modulating state (black line). (b) Event size and duration (integrated area above and below 0 in Figure 10a), scaled so the largest El Niño $= -1$ (Units: SOI index $\times$ time). Very long duration La Niña occur from 1955 to 1975 for $f_{65} > 0.1$ (vertical (horizontal) blue line in Figure 10b) (Figure 10a)). Prolonged El Niño occurs from 1975 to 2015 for $f_{65} < 0.1$ (horizontal blue line in Figure 10b)).

vice versa. The magnitude of this frequency state causes the duration of El Niño and La Niña to lengthen for f_{65} between 0 and ± 0.12. As the state reaches its maximum above ± 0.18 the event durations become compressed which will appear as higher variability in timing and duration of both El Niño and La Niña event types. Then as the state goes from its maxima back to zero, the duration of events lengthen again. For the Pacific basin ENSO process, we take {61–75, 180} years as representing the long-term cycle (LT). Phase transition components: $h(t)$ to $h(t+\ \tau)$ in Figure 9d with $\tau = 1$ year show the yearly phase transition characteristic of equation (11). These are derived from the T94 bifurcation plot in Figure 3a where $\kappa = 1.875$. It shows that based on the T94 tropical ENSO theory that strong El Niño events tend to persist for a second year but otherwise the ENSO El Niño phase moves into its La Niña phase.

For the Heartbeat of the Southern Oscillation attractor, we also obtain the ENSO modulation characteristic (Figure 10) to help explain regular interdecadal changes. The modulation characteristic represents the total the event size and duration as the attractor varies across the 65 year frequency state. The event size and duration is the integrated event area above zero (La Niña) and below zero (El Niño) of the attractor (Figure 10a) with units [SOI index $\times$ time] scaled so the strongest El Niño has value -1. Figure 10b shows the event size and duration verses the 65 year frequency state. The modulation characteristic of the attractor has a nonlinear threshold at $f_{65}=0.1$. Above this value (1950–1972) there are weak El Niño and very strong La Niña. Below this threshold (1972–2016), the El Niño events become stronger. For El Niño, the ratio of event size and duration of events after the shift verses before is 2:1. The La Niña event size and duration ratio across the shift is about 12:1 with the nonlinear threshold being very apparent for the persistent La Niña. We also note that the four strongest La Niña all sum to 5.0 event size and duration units and the seven strongest El Niño sum to -5.7. The small magnitude of the net effect (–0.7) is consistent with the stability of this attractor.

3.6. Evidence of Time Varying Atmospheric-Oceanic Coupling

The Heartbeat of the Southern Oscillation is the stable tropical ENSO attractor. It has periodic and subharmonic resonance characteristics with both short-term and long-term components. It corresponds to the periodic components of the El Niño and La Niña cycle. The T94 tropical ENSO representation of ENSO by the delay oscillator mechanism (equation (11)) allow for changes to the atmospheric-oceanic coupling term κ. We consider a decomposition of the coupling term using the f^{δ}_{SOI} frequency state evidence into the Short-Term Heartbeat (ST_{HB}), Chaotic and Long-Term-Heartbeat (LT_{HB}) components as specified in equation (13). This helps more generally to develop an understanding of how coupling could vary. The tropical ENSO theory gives a period-three attractor which is the high frequency component of the tropical El Niño (one branch) and La Niña cycle (two branches). This is shown in Figure 3a. With the T94 equation the low frequency part is contained within the $3n^2 + I$ intermittency part of the resonance feature. To determine the relative κ values in the equation (13) decomposition, we compare the signal variance and structural

properties of the f^s_{SOI} frequency state with the equivalent properties of the T94 resonance characteristic (Figure 3a). The combined high frequency states $f_{2.5}+f_5$ correspond to $\kappa^{ST_{HB}} = 1.33$ in Figure 3a. This is where the underlying period-three attractor is clearly defined by the ENSO system resonance property. Based on the Southern Oscillation frequency state model, it follows from equation (14) that the mean of the LT Heartbeat oscillation term $\delta\kappa(t)^{LT_{HB}}$ will be zero because $\int_{1951}^{2016} f_{65}\ dt = 0$, i.e., the low frequency component precesses equally in time across its positive and negative phases for the SOI data set. We see from Figure 3a that the variability of $h(t)$ in the bifurcation characteristic increases as κ goes from 1.33 to 2.13 indicating that the signal variance is lower in the periodic region than in the weakly chaotic region. To establish $\delta\kappa^{Chaotic}$, we assess its value using the variability property with the Root-Mean-Square (RMS) of the simulated T94 tropical ENSO processes signal and contrast this with the RMS of the Short-Term Heartbeat frequency state component of the Southern Oscillation. This shows the RMS ratio $[f_{2.5}+f_5]/\text{RMS}\ [f^s_{SOI}] = 0.72$. By varying κ, we found when $\kappa = 1.875$ then RMS ratio $[h(t_s;\kappa = 1.33)]/\text{RMS}\ [h(t_s;\kappa = 1.875)] = 0.714$. It follows that the current average of the atmospheric-oceanic coupling parameter is $\kappa^{ST_{HB}} + \delta\kappa^{Chaotic} \cong 1.875$ implying that $\delta\kappa^{Chaotic} \cong 1.875 - 1.330 = 0.545$. It is more of a challenge to establish the amplitude of the variability of $\delta\kappa(t)^{LT_{HB}}$. *Li et al.* [2013] examined the presence of interdecadal variance due to stochastic noise by analyzing the SSTA using a 31 year averaging approach. They suggest that much of twentieth century ENSO variance stands out from random variability simply due to stochastic processes. We found (supporting information Figures S1 and S2), that there are combined 120 and 180 year cycles in the variability. This cyclic variability corresponds to a long-term and slow oscillation represented by $\delta\kappa(t)^{LT_{HB}}$. The low variability corresponds to a reducing coupling value, moving the system toward a lower variance part of the T94 bifurcation characteristic and vice versa. As historically the lower variance parts of the process have not resulted in nonchaotic mode locked resonance cycles, which would appear for $\kappa < 1.781$ (approximate upper threshold κ value for stable resonance states in Figure 3b), we treat this as the lower range of the coupling variability. By assuming symmetry around the mean value of 1.875, the range of $\delta\kappa(t)^{LT_{HB}}$ varies between 1.781 and 1.969. So we define $\delta\kappa(t)^{LT_{HB}} = 0.094 g(\cos\omega_{LT_{HB}} t)$ with $g(\ldots)$ representing the combination of the Long-Term Heartbeat part of the attractor. Therefore, the time varying coupling coefficient can be of the form:

$$\kappa(t) \sim 1.33 + 0.545 + 0.094\ g(\cos\omega_{LT_{HB}} t) \tag{17}$$

3.7. Projection of Future ENSO State

We have shown that the frequency states represent the underlying mechanistic resonance conditions of the ENSO process and these appear to have a negligible trend. Just as in the case of future tidal prediction, we can project the ENSO frequency states. The assumption here is that the dominant eigenvalues of the process will not change their value into the future. With DFSA such a future projection is valid within the thresholds $A_{\pm}$ defined in equation (7). The variation outside these thresholds also helps explain the observed stability of the ENSO process hysteresis in its extreme range. In Figure 11, the frequency state projection to 2100 is given. The Southern Oscillation Index model shows with the positive and negative f_{65} state, that we can expect prolonged La Niña over the period 2018–2040, with this modulated by two cycles of the f_{12} year frequency state (Figure 11a). During the negative f_{65} phase, we expect large El Niño events over the period 2050–2070. Then going from 2080 to 2100 are two decades of prolonged La Niña. The NPIA frequency state projection (Figure 11b) shows much the same. This indicates that we should be able to clearly see the NPIA change its sign, the next positive to negative transition due to occur in the 2040s decade. The SSTA analysis projected forward to 2100 includes the f_{180} year frequency state. In 2016, the total frequency state appears to be at the height of its stable positive range. This indicates that with the combined frequency states of the system, that we have reached a type of combined maxima in the SSTA temperatures. As such over the next few years and decade a general Pacific SST cooling should become apparent. The combination of $f_{75} + f_{180}$ modulates the projection resulting in a two events that exceed the SSTA > -0.06°C threshold (the first one in 2040 and the second one in 2060). The f^s_{SSTA} model anticipates that there will be a positive to negative transition in about 2050, with Pacific SST temperatures reducing markedly during the prolonged La Niña period from 2080 to 2100.

3.8. Hysteresis of Low Frequency ENSO State and Threshold Extremes

In Figure 12, we show how the proportion of low and high temperature extremes derived from the SSTA frequency states vary by century. There are centuries with high temperature extremes {1300, 1400, 1600, 1800},

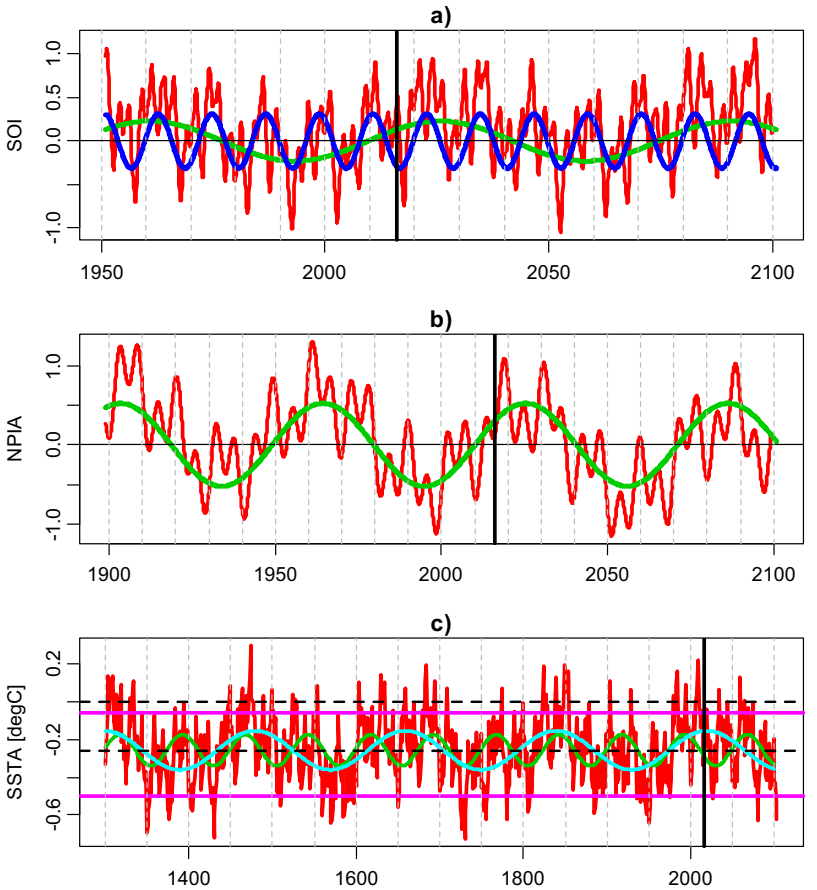

Figure 11. The projection of future ENSO frequency states to 2100. Solid vertical line is 2016 (January). (a) Southern Oscillation model (red line) with 12 year (blue line) and 65 year (green line) frequency states. (b) North Pacific Index Anomaly model (red line) with 61 year (green line) frequency states. (c) SSTA model (red line) with 75 year (green line) and 180 year (light blue line) frequency states. A prolonged La Niña period is expected over 2020–2040 corresponding the positive (negative) phase of the 60–65 (75) year NPIA and SOI (SSTA) frequency states.

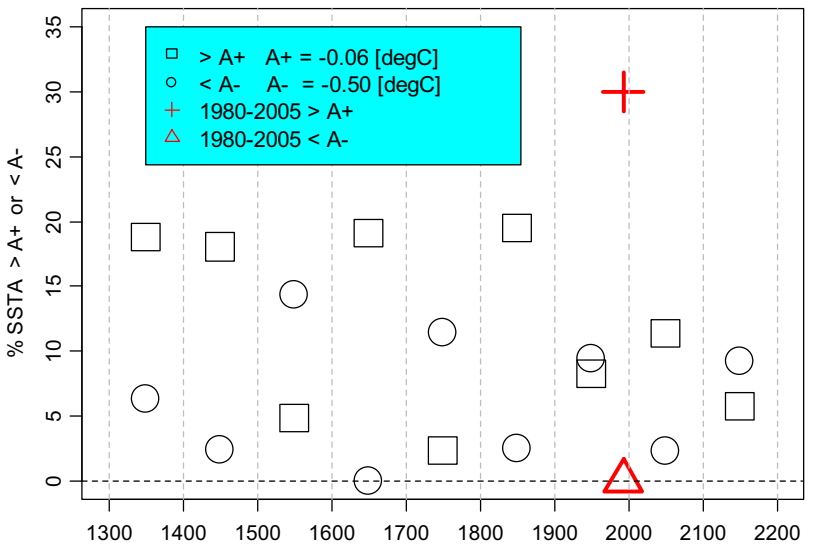

Figure 12. Centennial proportion of SSTA threshold crossing for ENSO SSTA frequency state model (including projection to 2200); 1900 instrumental period is a mixture of hot and cold extremes and appears very warm in the most recent 25 years. As a comparison the most recent 1980–2005 25 year data period are shown in red. This shows excessively warm and cold epochs. The warm period persists in 2000s and more cold extremes come in 2100s. Each century has a differing characteristic.

low temperature extremes {1500, 1700} and currently for 1900 a balanced mixture of the two. The recent warming (1980–2005 time window) plotted on this figure suggests that the ENSO has apparently moved outside the threshold levels and appears as a warm phase. These low frequency threshold exceedances, derived from paleoproxy DFSA estimates, suggest that each century looks different. This is because the regular low frequency modes are not exactly repeating every 100 years. So each century has differing ENSO properties, being warm, or cold or a mixture of both. The regularity of the ENSO attractor state indicates this can be an example of a regular and moving baseline. It could be the case that the hysteresis of the system may be changed if current warm phase persists, such that future frequency states would become modified. The future projection to 2200, assuming the frequency states remain stable, give a warm century for the 2000s and a mixture for the 2100s.

4. Discussion

Current discussions regarding the ENSO system inevitably concern the impact of climate change and the coupling of the ocean-atmosphere system. Changes could happen for example through adaptation of the intensity of the Walker circulation or changes to the equatorial thermal stratification gradients. Using a Dominant Frequency State Analysis and the universal eigenvalue decay characteristic of the T94 tropical ENSO delay oscillator we show that the observed ENSO process can exhibit periodic resonances with a high and low frequency subharmonic structure. Our analysis shows that both the 2–8 year cyclic and longer term 10–200 year cyclic resonances are a feature of ENSO. The longer-term resonances will be due to thermal readjustment and repeated wave combinations that persist over many years across the Pacific basin. By relaxing the assumption of no extratropical interaction, we have examined the existence and implications of low and high frequency resonance and coupling interactions across the whole Pacific basin. The departures from the tropical ENSO process form the main thesis of this work. We find that the tropical ENSO process also has a 65 year frequency state that together with the 2.5 and 5 year frequency states form the tropical ENSO attractor that we call the Heartbeat of the Southern Oscillation. This description is also consistent with the well-established seasonal forcing frequency being entrained with the ENSO resonance [*Tziperman et al.*, 1994]. The 2.5 plus 5 year term is mode locked with the seasonal cycle in a ratio 5:1. For the simple delay oscillator (T94) low frequency structure can appear in the intermittency part of the $3n^2+1$ characteristic. Our analysis of the logistic and simple delay oscillator class shows that a subharmonic decay of 0.99 dB per subharmonic would present a low frequency mode as intermittency. The DFSA eigenvalue analysis of the SOI actually finds a subharmonic decay rate of 0.44 dB per subharmonic for this attractor (but the 0.99 dB value is still within the 95% confidence interval of the eigenvalue spectrum). The low frequency mode could be intermittency, a long-term frequency state or a combination of these.

The Heartbeat of the Southern Oscillation attractor also gives an ENSO modulation characteristic. The repeating event size and duration is a nonlinear characteristic with prolonged La Niña (and weak El Niño) for 20 years while $f_{65} > 0.1$ and strong El Niño (and weak La Niña) for 40 years when the frequency state is present for $f_{65} < 0.1$. The existence of these lower frequency states is also corroborated in the extratropical analysis of the NPIA and the paleoproxy analysis of the SSTA. The implication of the low frequency structure assessed with DFSA is that while the T94 tropical ENSO delay oscillator explains well the equatorial process of up to 8 years the ability to extend the simple ENSO model to the basin scale using low frequency intermittency and incorporate longer-term frequency states is limited. The T94 tropical ENSO delay oscillator representation is most likely not sufficiently general enough to fully represent the Pacific basin ENSO coupled tropical and extratropical process. The ENSO process that the Pacific basin trees (measured with the paleoproxy record) have experienced over the last 700 years is likely to be a hybrid combination of the tropical Heartbeat of the Southern Oscillation attractor and extratropical interaction with the subtropical gyres that exhibit the slow ocean dynamic adjustment phenomenon. A basin scale ENSO process understanding similar in form to the tropical delay oscillator should be developed. This analysis helps provide a step toward developing this basin scale ENSO representation from the perspective of the eigenvalue characteristics derived from time series. Overall, our analysis of Pacific ENSO data with DFSA and the T94 tropical ENSO eigenvalue characteristics show the following:

A. The tropical ENSO system follows a type of universal period doubling cascade route to chaos that includes low frequency modes mediated by extratropical coupling.

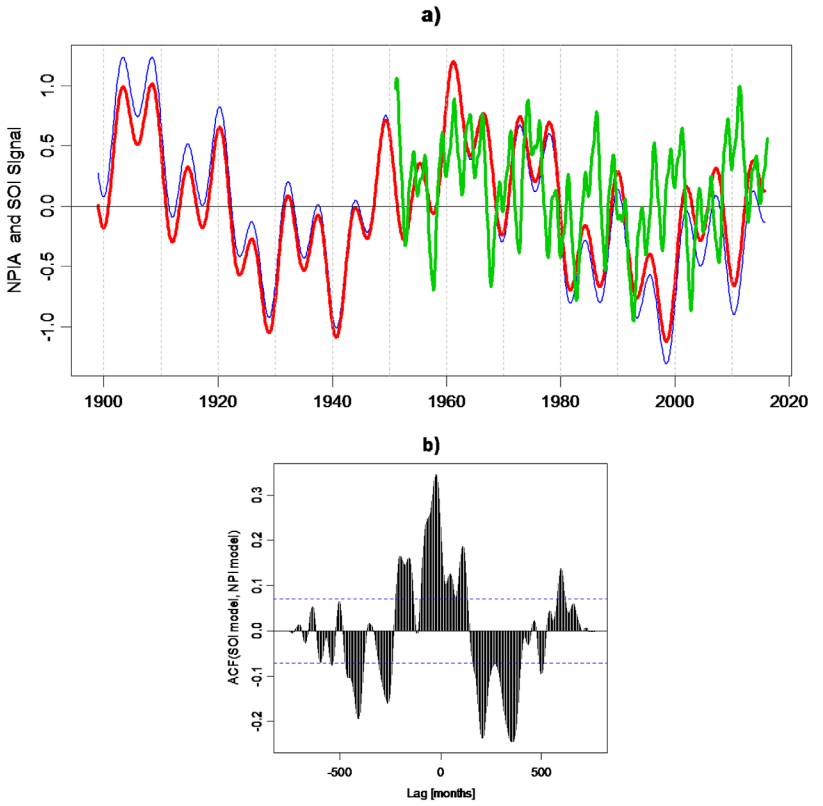

Figure 13. (a) Frequency state models of Southern Oscillation (green line) and North Pacific Index Anomaly (red line) The blue line is the addition of a linear trend (estimated to be negative) to the NPIA. (b) Cross correlation of SOI model and NPIA model: shows an interim identification of the slow ocean dynamic adjustment memory that links the equatorial and North Pacific locations. The positive lag structure indicates short-term positive correlation (immediate 2–8 year ENSO event response) and long-term negative and later positive fluctuations (15–50 years). The negative lag structure also shows previous NPIA events influence the SOI signal. The total ENSO system is connected at a Pacific basin scale.

B. For the tropical ENSO T94 characteristic the three underlying branches corresponding to El Niño (top branch, thermocline deepening) and La Niña (bottom two branches, thermocline shallowing) with these phases still apparent in the weakly chaotic regime $\kappa > 1.78$. These three branches are consistent with the $f_{2.5}$ and f_5 Heartbeat of the Southern Oscillation attractor frequency states.
C. Longer-term resonance cycles (10–200 years) are partly a feature of the ENSO process with the f_{65} frequency state modulating the high frequency states of the heartbeat attractor.

Our analysis includes an assessment of the tropical and extratropical coupling properties that result in basin scale ENSO features. The subtropical gyres respond to external system input changes with the slow dynamic adjustment memory mechanism [*Jin*, 1997]. The frequency states f^s_{SOI} and f^s_{NPIA} (from equations (14) and (15)) are shown in Figure 13a). The form of the memory relationship that connects the tropical and extratropical (North) Pacific is assessed using the cross-correlation function CCF(f^s_{SOI}, f^s_{NPIA}) shown in Figure 13b. This gives an interim identification of the slow ocean dynamic adjustment memory. The positive-negative leading and lagged structure is indicative of the tropical and extratropical ENSO feedback and coupled processes across the Pacific basin. The DFSA shows that ENSO is a basin scale phenomenon with specific tropical and extratropical mechanisms. The long period cycles represent the rebalancing of the thermal budget across the Pacific. For example with extremely large ENSO events (such as a 1-in-50 year El Niño event) a huge amount of thermal heat is rapidly transported from the west Pacific warm pool to the eastern Pacific equatorial region and then the system slowly rebalances the thermal budget back to the west Pacific warm pool. These delays occur both rapidly along the equator and are slowly varying away from the equator. The slow ocean dynamic adjustment mechanism of the subtropical gyres and the related extratropical atmosphere-ocean coupling act to help regulate the system. Our analysis suggests that for the Pacific basin it can take decades and interdecadal time periods to fully rebalance the thermal ENSO budget. This

supports a teleconnection ocean bridge hypothesis of *Zhang et al.* [1998] of extratropical to tropical thermal transport. Our finding is consistent with recent work on correlations between the tropical ENSO signal and Northern Pacific low frequency longitudinal variation in the atmospheric weather patterns. The 1950–1978 (1978–2010) period corresponds to the NPIA positive (negative) phases. During the positive NPIA phase, there is a reported negative (positive) correlation between the Northern (Western) extratropical SSTA's [*He et al.*, 2013]. During the NPIA negative phase, the positive Western correlation weakens and the Northern negative correlation pattern widens its spatial coverage. This implies there is a strengthened relationship between tropical ENSO and Northern extratropical SSTA's. There is also a reduced East Asian Winter Monsoon and tropical ENSO connection and an intensified EAWM connection to the Arctic Oscillation during this period corresponding to the NPIA negative phase [*Wang and He*, 2012]. Our results show that during 2010–2040 the NPIA is in a positive phase (Figure 11b). Based on the tropical and extratropical ENSO coupling dynamics, during the current NPIA positive phase we expect to see a strengthened ENSO-EAWM connection (with a reduced EAWM-Arctic Oscillation connection), the extratropical Western negative correlation pattern with tropical ENSO to strengthen and the extratropical Northern positive correlation of tropical ENSO with SSTA to weaken. By confronting the *Cane and Zebiak* [1985] assumption of nonextratropical influence, we have used the north Pacific instrumental NPIA record to assess the interaction. We do not have an equivalently long instrumental record of the southern Pacific. This is likely to have similarity to the North, but also differences due to basin width and ocean contact with thermohaline flow near to the Antarctic. The SSTA paleoproxy record represents the ENSO signal for the whole of the Pacific basin over 700 years. The dominant frequencies we observe in this represent tropical, Northern and Southern Pacific characteristics. The 13 year frequency state is likely to be a combination of the 12 year tropical effect and the 14 year subtropical cycle. The magnitude of the eigenvalues for the basin scale analysis suggests that the extratropical effects are large. This also shows that the higher frequency 2–8 year tropical ENSO effect is present in the basin scale signal. From the perspective of the basin scale tree ring growth the tropical ENSO impact is filtered by the extratropical effect so the lower frequency modes appear more dominant, yet retain the tropical ENSO subharmonic decay structure. The Heartbeat of the Southern Oscillation attractor is observed at a basin scale.

We have found that there is virtually no evidence of an underlying seven century long-term trend in the frequency states of the ENSO process. We find that the system is dominated by its cyclic frequency states. This implies that Pacific and other planetary climatic regime shifts that are ENSO dependent are most likely to be linked to the combination of changes in the positive and negative phases of the ENSO longer-term cycles. Due to the planetary fluid-dynamic nature of this system, the ENSO process exists with semi-rigid boundary conditions. The collective effects of land masses around the Pacific basin, the equatorial Pacific waveguide and coupling between atmosphere-ocean latitudinal zones all provide the ENSO system boundary conditions. Other global climatic system interactions with ENSO also form part of the boundary condition properties. The dominant frequency states of the ENSO embed these boundary conditions and include nonlinear thresholds. Any changes to these boundary conditions could alter the stability of the ENSO process eigenvalues and eigenvectors and result in a change of hysteresis. Where the skill levels hold, the frequency states are the stable ENSO resonances of the system. Where the skill reduces the specific characteristics of the semi-rigid boundaries could alter or distort the frequency states. The SOI skill levels are highest with the NPIA and then the SSTA being slightly less well defined (see Figures 5c, 5f, and 5i). This suggests that the boundary conditions have a larger impact as the spatial scale of the system grows.

With the basin scale paleoproxy SSTA data the increasing temperature events start to loose skill for SSTA events with temperatures of -0.06°C. This includes the recent 1970–2005 period where both the 180 and 75 year frequency state have combined to create a doubly positive state of these two cycles. Model skill for lower temperature variations has a larger negative frequency state range than for positive state increases (it is easier to go colder than hotter and retain frequency state skill). For the SSTA, the proportion of warm and cold threshold exceedances change by century, some being warmer, and others colder. For the 20th century the proportion of warm and cold events are both about 10% of the signal and this is different to the extremes of the last 600 years. The recent 25 years (1980–2005 in the record) appear excessively warm and this is consistent with current instrumental measurements and records. Work by *Liu* [2002] suggested that ENSO mode amplitude can also be influenced by external forcing such as insolation or monsoon winds and could help explain paleoproxy time scale ENSO suppression during the Holocene. The DFSA analysis of the

700 year SSTA record shows that the ENSO system reverts back to the stable frequency state cycles following high temperature threshold crossings (see Figure 5h) in 1310, 1470, 1630, 1690, and 1830–1860. Above −0.06°C, the SSTA signal appears to recover some frequency state skill, which may be additional evidence of longer-term hysteresis stability. The Heartbeat of the Southern Oscillation is the stable tropical ENSO system attractor. The evidence implies that the observed system can self-regulate itself, through the mechanisms discussed here and has in the past 700 years repeatedly reverted back to the stable attractor ENSO process. This means that the ENSO system, including its boundary conditions, has been in a naturally balanced thermodynamic equilibrium for seven centuries.

Given the stability of the frequency states the current rare combination of two in-phase positive 75 and 180 year SSTA cycles is unlikely to have pushed the ENSO system out of its stable attractor space. Our analysis shows that over the coming years the trajectory is most likely to continue around the Heartbeat of the Southern Oscillation stable attractor and so the current SSTA temperature level should generally reduce going into the next 30 years. The system has a natural elasticity or stable hysteresis that helps the resonances to move from its extreme range back into the range of stable ENSO frequency states.

A key part of the tropical ENSO phenomenon is the strength and dynamic form of the ocean and atmosphere coupling κ. Based on the simple T94 delay oscillator the current tropical ENSO resonance characteristic has value $\kappa = 1.875$. This could imply that there is flexibility for the Pacific ENSO system to adapt even in the case of major changes to the semi-rigid boundary conditions. In response to a major change, κ could increase making the tropical ENSO system more intermittent both increasing the resonance variability and LT_{HB} duration. Alternatively it could act to decrease κ into a set of purely periodic attractor resonances with lower system variability. However, an extended basin scale ENSO representation is called for that incorporates the eigenvalue stability characteristics discussed here so a more complete assessment of the stability of the basin scale ENSO phenomenon can be established.

5. Conclusions

We have applied a dynamic system analysis to study the ENSO phenomenon. This uses a highly accurate Dominant Frequency State Analysis approach to explain the deterministic and chaotic nature of the ENSO climatic process. This has used 100 years of instrumental observational time series data, 700 years of paleoproxy time series data with a combined Pacific basin and equatorial scale resolution, linked together with simulations of the tropical ENSO delay oscillator theory.

Our analysis shows that the tropical ENSO climatic resonances have a stable attractor. We call this attractor the Heartbeat of the Southern Oscillation which has mode locked high (2.5 and 5 year) and low frequency (65 year) resonance coupling consistent a class of dynamic system that has a periodic subharmonic form of chaos and low frequency modulation that can include intermittency. We have shown that the basin scale ENSO process has large and stable long-term climatic oscillations lasting between 10 and 200 years which have been regularly occurring over the past seven centuries. Our analysis does not find an underlying trend in the ENSO process and there is actually a large degree of system hysteresis stability dominated by the cyclic frequency states.

Acknowledgments
We thank researchers at Plymouth Marine Laboratory (PML) for helpful discussions on Dominant Frequency State Analysis of earth system time series to help interpret the ENSO long-term mechanisms and fluctuations in biogeochemical climate systems. We also thank two anonymous reviewers and the editor for comments that helped focus the methodological precision and implications of this work in climate science. The time series analysis and simulation codes for this paper is available from the R Core Team open access links (package TSA and deSolve): www.R-project.org. All the data is freely available and the open access links given in the data section. For the SOI: http://www.ncdc.noaa.gov/teleconnections/enso/indicators/soi/. For the NPIA: http://www.esrl.noaa.gov/psd/gcos_wgsp/Timeseries/NP/. For the SSTA: ftp://ftp.ncdc.noaa.gov/pub/data/paleo/treering/reconstructions/enso-li2013.txt. This research was supported by PML and the NERC National Capability in Modelling program at PML.

References

Allen, I. J., T. Smyth, J. R. Siddorn, and M. Holt (2008), How well can we forecast high biomass algal bloom events in a eutrophic coastal sea?, *Harmful Algae*, *8*(1), 70–76, doi:10.1016/j.hal.2008.08.024.

An, S., and F. Jin (2004), Nonlinearity and asymmetry of ENSO, *J. Clim.*, *17*(12), 2399–2412, doi:10.1175/1520-0442(2004)017 < 2399:NAAOE>2.0.CO;2.

Andronov, T. E., and S. E. Khaikin (1937), *Theory of Oscillations* [in Russian], Moscow. [Engl. translation by S. Lefschetz (1949), Princeton Univ. Press, Princeton, N. J.]

Battisti, D., and A. C. Hirst (1989), Innterannual variability in tropical atmosphere-ocean model: Influence of the basic state, ocean geometry and nonlinearity, *J. Atmos. Sci.*, *46*, 1687–1712.

Battisti, D. S. (1995), Decade-to-century time-scale variability in the coupled atmosphere-ocean system: Modeling issues, in *The Natural Variability of the Climate System on the 10–100 Year Time Scales*, edited by D. G. Martinson et al., pp. 419–429, Natl. Acad. Press, Washington, D. C.

Bjerknes, J. (1969), Atmospheric teleconnections from the equatorial pacific, *Mon. Weather Rev.*, *97*(3), 163–172.

Bloomfield, P. (2000), Fourier analysis of time series, *Wiley Series in Probability and Statistics*, John Wiley & Sons, Inc., New York.

Box, G. E. P., and G. M. Jenkins (1970), *Time Series Analysis, Forecasting and Control*, Holden-Day, San Francisco, Calif.

Bruun, J. T., and J. A. Tawn (1998), Comparison of approaches for estimating the probability of coastal flooding, *Appl. Stat.*, *47*(3), 405–423.

Bruun, J. T., S. N. Evangelou, and C. J. Lambert (1995), Universal level statistics in the presence of Andreev scattering, *J. Phys. Cond. Matter*, *7*, 4033–4050, doi:10.1088/0953-8984/7/21/004.
Burgers, G., F.-F. Jin, and G. J. Oldenborgh (2005), The simplest ENSO recharge oscillator, *Geophys. Res. Lett.*, *32*, LI3706, doi:10.1029/2005GL022951.
Cane, M. A. (2005), The evolution of El Niño, past and future, *Earth Planet. Sci. Lett.*, *230*(3–4), 227–240, doi:10.1016/j.epsl.2004.12.003.
Cane, M. A., and S. E. Zebiak (1985), A theory for El Niño and the Southern Oscillation, *Science*, *228*, 1085–1087.
Chekroun, M. D., E. Simonnet, and M. Ghil (2011), Stochastic climate dynamics: Random attractors and time-dependent invariant measures, *Phys. D: Nonlinear Phenomena*, *240*(21), 1685–1700, doi:10.1016/j.physd.2011.06.005.
Coles, S. (2001), An introduction to statistical modelling of extreme values, in *Springer Series in Statistics*, Springer, London, U. K.
Dijkstra, H. A., and M. Ghil (2005), Low-frequency variability of the large-scale ocean circulation: A dynamical systems approach, *Rev. Geophys.*, *43*, RG3002, doi:10.1029/2002RG000122.
Feigenbaum, M. J. (1980), The metric universal properties of period doubling bifurcations and the spectrum for a route to turbulence, *Ann. N. Y. Acad. Sci.*, *357*, 330–336.
Ghil, M., et al. (2002), Advanced spectral methods for climatic time series, *Rev. Geophys.*, *40*(1), 1003, doi:10.1029/2000RG000092.
Glantz, M. H. (2001), *Current of Change: Impacts of El Niño and La Niña on Climate and Society*, Cambridge Univ. Press, Cambridge, U. K.
Hannachi, A., I. T. Jolliffe, and D. B. Stephenson (2007), Empirical orthogonal functions and related techniques in atmospheric science: A review, *Int. J. Climatol.*, *27*, 1119–1152, doi:10.1002/joc.1499.
He, S., H. Wang, and J. Liu (2013), Changes in the relationship between ENSO and Asia-Pacific midlatitude winter atmospheric circulation, *J. Clim.*, *26*, 3377–3393, doi:10.1175/JCLI-D-12-00355.1.
Hilborn, R. C. (2000), *Chaos and Nonlinear Dynamics*, 2nd ed., Oxford Univ. Press, Oxford, U. K.
Hoskins, B. J., and D. J. Karoly (1981), The steady linear response of a spherical atmosphere to thermal and orographic forcing, *J. Atmos. Sci.*, *38*(6), 1179–1196, doi:10.1175/1520-0469(1981)038 < 1179:TSLROA>2.0.CO;2.
Jin, F.-F. (1997), A theory of interdecadal climate variability of the North Pacific ocean-atmosphere system, *J. Clim.*, *10*, 1821–1835.
Jin, F.-F., D. Neelin, and M. Ghil (1994), El Nino on the devil's staircase: Annual subharmonic steps to chaos, *Science*, *264*(5155), 70–72.
Kaplan, A., M. A. Cane, Y. Kushnir, A. C. Clement, M. B. Blumenthal, and B. Rajagapalan (1998), Analyses of global sea surface temperature 1856–1991, *J. Geophys. Res.*, *103*, 18,567–18,589.
Latif, M., D. Anderson, T. Barnett, M. Cane, R. Kleeman, A. Leetmaa, J. O'Brien, A. Rosati, and E. Schneider (1998), A review of the predictability and prediction of ENSO, *J. Geophys. Res.*, *103*, 375–393, doi:10.1029/97JC03413.
Li, J., et al. (2013), El Niño modulations over the past seven centuries, *Nat. Clim. Change*, *3*, 822–826, doi:10.1038/NCLIMATE1936.
Liu, Z. (2002), A simple model study of ENSO suppression by external periodic forcing, *J. Clim.*, *15*, 1088–1098.
Lüdecke, H.-J., A. Hempelmann, and C. O. Weiss (2013), Multiperiodic climate dynamics: Spectral analysis of long-term instrumental and proxy temperature records, *Clim. Past*, *9*, 447–452
Mann, M. E., and J. M. Lees (1996), Robust estimation of background noise and signal detection in climatic time series, *Clim. Change*, *33*(3), 409–445, doi:10.1007/BF00142586.
McPhaden, M. J. (1999), Genesis and evolution of the 1997–98 El Niño, *Science*, *283*, 950–954, doi:10.1126/science.283.5404.950.
McPhaden, M. J., et al. (1998), The Tropical Ocean-Global Atmosphere observing system: A decade of progress, *J. Geophys. Res.*, *103*, 14,169–14,240, doi:10.1029/97JC02906.
McPhaden, M. J., S. E. Zebiak, and M. H. Glantz (2006), ENSO as an integrating concept in Earth science, *Science*, *314*, 1740–1745, doi:10.1126/science.1132588.
Minobe, S. (1999), Resonance in bidecadal and pentadecadal climate oscillations over the North Pacific: Role in climatic regime shifts, *Geophys. Res. Lett.*, *26*, 855–858.
Münnich, M., M. A. Cane, and S. E. Zebiak (1991), A study of self-excited oscillations of the tropical ocean-atmosphere system. Part II: Nonlinear cases, *J. Atmos. Sci.*, *48*(10), 1238–1248, doi:10.1175/1520-0469(1991)048 < 1238:ASOSEO>2.0.CO;2.
Neelin, J. D., D. S. Battisti, A. C. Hirst, F.-F. Jin, Y. Wakata, T. Yamagata, and S. E. Zebiak (1998), ENSO theory, *J. Geophys. Res.*, *103*, 261–290, doi:10.1029/97JC03424.
Pawitan, Y. (2013), *In All Likelihood: Statistical Modelling and Inference Using Likelihood*, Oxford Univ. Press, Oxford, U. K.
R Core Team (2014), *R: A Language and Environment for Statistical Computing*, R Found. for Stat. Comput., Vienna. [Available at http://www.R-project.org/.]
Rasmusson, E. M., X. Wang, and C. F. Ropelewski (1990), The biennial component of ENSO variability, *J. Mar. Syst.*, *1*, 71–96.
Scheffer, M. (2009), *Critical Transitions in Nature and Society*, Princeton Univ. Press, N. J.
Scheffer, M., J. Bascompte, W. A. Brock, V. Brovkin, S. R. Carpenter, V. Dakos, H. Held, E. van Nes, M. Rietkerk, and G. Sugihara (2009), Early-warning signals for critical transitions, *Nature*, *461*, 53–59, doi:10.1038/nature08227.
Sponberg, K. (1999), *Compendium of Climatological Impacts*, Natl. Oceanic and Atmos. Admin., Washington, D. C.
Suarez, M., and P. S. Schopf (1988), A delayed action oscillator for ENSO, *J. Atmos. Sci.*, *45*, 3283–3287.
Tong, H. (1990), Non-linear time series, a dynamical system approach, *Oxford Statistical Science Series 6*, Oxford Univ. Press, New York.
Trenberth, K. E., and D. P. Stepaniak (2001), Indices of El Niño evolution, *J. Clim.*, *14*(8), 1697–1701, doi:10.1175/1520-0442(2001)014 < 1697:LIOENO>2.0.CO;2.
Trenberth, K. E., G. W. Branstator, D. Karoly, A. Kumar, N.-C. Lau, and C. Ropelewski (1998), Progress during TOGA in understanding and modelling global teleconnections associated with tropical sea surface temperature anomalies, *J. Geophys. Res.*, *103*, 14,291–14,324, doi:10.1029/97JC01444.
Tziperman, E., L. Stone, M. A. Cane, and H. Jarosh (1994), El Niño chaos: Overlapping of resonances between the seasonal cycle and the Pacific Ocean-Atmosphere oscillator, *Science*, *264*, 72–74.
Tziperman, E., M. A. Cane, and S. E. Zebiak (1995), Irregularity and locking to the seasonal cycle in an ENSO prediction model as explained by the quasi-periodicity route to chaos, *J. Atmos. Sci.*, *52*, 293–305.
Wang, H. J., and S. P. He (2012), Weakening relationship between East Asian Winter Monsoon and ENSO after mid-1970s, *Chin. Sci. Bull.*, *57*, 3535–3540, doi:10.1007/s11434-012-5285-x.
Wolter, K., and M. S. Timlin (2011), El Niño/Southern Oscillation behaviour since 1871 as diagnosed in an extended multivariate ENSO index (MEI.ext), *Int. J. Climatol.*, *31*, 1074–1087, doi:10.1002/joc.2336.
Yeh, S. W., J.-S. Kug, B. Dewitte, M.-H. Kwon, B. P. Kirtman, and F.-F. Jin (2009), El Niño in a changing climate, *Nature*, *461*, 511–514, doi:10.1038/nature08316.
Young, P. C. (2011), *Recursive Estimation and Time-Series Analysis*, 2nd ed., Springer, Berlin.

Young, P. C., P. McKenna, and J. T. Bruun (2001), Identification of non-linear stochastic systems by state dependent parameter estimation, *Int. J. Control*, *74*(18), 1837–1857, doi:10.1080/00207170110089824.

Zhang, R.-H., L. M. Rothstein, and A. J. Busalacchi (1998), Origin of upper-ocean warming and El Nino change on decadal time scales in the Tropical Pacific Ocean, *Nature*, *391*, 879–883.

Zhang, Y., J. M. Wallace, and D. S. Battisti (1997), ENSO-like interdecadal variability: 1900–93, *J. Clim.*, *10*(5), 1004–1020, doi:10.1175/1520-0442(1997)010 < 1004:ELIV>2.0.CO;2.